# Profile-Encoding Reconstruction for Multiple-Acquisition Balanced Steady-State Free Precession (bSSFP) Imaging

| | |
|---|---|
| Journal: | *Magnetic Resonance in Medicine* |
| Manuscript ID | MRM-16-17010.R2 |
| Wiley - Manuscript type: | Full Paper |
| Date Submitted by the Author: | n/a |
| Complete List of Authors: | Ilicak, Efe; Bilkent University, Electrical and Electronics Engineering<br>Senel, Lutfi; Bilkent University, Department of Electrical and Electronics Engineering<br>Biyik, Erdem; Bilkent University, Department of Electrical and Electronics Engineering<br>Çukur, Tolga; Bilkent University, Department of Electrical and Electronics Engineering; Bilkent University, National Magnetic Resonance Research Center (UMRAM); Bilkent University, Neuroscience Program |
| Research Type: | Compressed sensing < Reconstruction < Technique Development < Technical Research, Reconstruction < Technique Development < Technical Research |
| Research Focus: | No specific tissue or organ focus |
| | |

# Profile-Encoding Reconstruction for Multiple-Acquisition Balanced Steady-State Free Precession (bSSFP) Imaging

Efe Ilicak[1,2], Lutfi Kerem Senel[1], Erdem Biyik[1], Tolga Çukur[1,2,3]

[1]Department of Electrical and Electronics Engineering, Bilkent University, Ankara, Turkey

[2]National Magnetic Resonance Research Center (UMRAM), Bilkent University, Ankara, Turkey

[3]Neuroscience Program, Bilkent University, Ankara, Turkey

*Running title:* Profile-Encoding Reconstruction for Multiple-Acquisition bSSFP

*Address correspondence to:*
Tolga Çukur
Department of Electrical and Electronics Engineering, Room 304
Bilkent University
Ankara, TR-06800, Turkey
TEL: +90 (312) 290-1164
E-MAIL: cukur@ee.bilkent.edu.tr

This work was supported in part by a Marie Curie Actions Career Integration Grant (PCIG13-GA-2013-618101), by a European Molecular Biology Organization Installation Grant (IG 3028), and by the Turkish Academy of Sciences through a TUBA-GEBIP 2015 fellowship awarded to T. Çukur.

Word Count: 190 (abstract), 5000 (body)
Figure and Table Count: 10

Revised submission on September 2, 2016 to *Magnetic Resonance in Medicine*.

## Abstract

**Purpose:** The scan-efficiency in multiple-acquisition bSSFP imaging can be maintained by accelerating and reconstructing each phase-cycled acquisition individually, but this strategy ignores correlated structural information among acquisitions. Here an improved acceleration framework is proposed that jointly processes undersampled data across N phase cycles.

**Methods:** Phase-cycled imaging is cast as a profile-encoding problem, modeling each image as an artifact-free image multiplied with a distinct bSSFP profile. A profile-encoding reconstruction (PE-SSFP) is employed to recover missing data by enforcing joint sparsity and total-variation penalties across phase cycles. PE-SSFP is compared with individual compressed-sensing (iCS) and parallel-imaging (ESPIRiT) reconstructions.

**Results:** In the brain and the knee, PE-SSFP yields improved image quality compared to iCS and other tested methods particularly for higher N values. On average, PE-SSFP improves peak SNR by 3.8±3.0 dB (mean±s.e. across N=2-8) and structural similarity by 1.4±1.2% over iCS, and peak SNR by 5.6±0.7 dB and structural similarity by 7.1±0.5% over ESPIRiT.

**Conclusion:** PE-SSFP attains improved image quality and preservation of high-spatial-frequency information at high acceleration factors, compared to conventional reconstructions. PE-SSFP is a promising technique for scan-efficient bSSFP imaging with improved reliability against field inhomogeneity.

**Keywords: SSFP, banding artifact, magnetization profile, compressed sensing, encoding, reconstruction**

# Introduction

Balanced steady-state free precession (bSSFP) sequences provide relatively high magnetization levels for repetition times (TR) on the order of several milliseconds (1). As such, they have found use in rapid imaging involving both dynamic (2–6) and high-spatial-resolution static acquisitions (7–11). One critical concern, however, is that the bSSFP magnetization profile yields increased sensitivity to magnetic field inhomogeneities and signal voids at particular off-resonance frequencies (1). In turn, this profile can lead to excessive banding artifacts at high field strengths, with long TRs, and in complex tissue geometries.

Several innovative methods were previously proposed to alleviate bSSFP banding artifacts. These methods include modified pulse sequences that reshape magnetization profiles (12–15), advanced shimming procedures that limit field inhomogeneity (16), physical signal models to remove frequency sensitivity (17, 18), and the commonly used multiple-acquisition methods that combine several phase-cycled images with nonoverlapping banding artifacts to improve signal homogeneity (19–24). These approaches typically compromise between artifact reduction and scan efficiency. For instance, residual banding artifacts in multiple-acquisition methods can be reduced by increasing the number of phase cycles (N). However, with higher N, the overall scan time is considerably prolonged.

To mitigate banding artifacts while maintaining scan efficiency, two recent studies proposed to accelerate phase-cycled bSSFP acquisitions (25, 26). In the first study (25), we leveraged individual compressed-sensing (CS) reconstructions to recover nonacquired bSSFP data for each phase cycle separately (27–29). In the second study (26), individual acquisitions were instead accelerated via simultaneous multi-slice imaging. While high image quality was demonstrated for low acceleration factors (around 2-4), data from separate phase-cycles were reconstructed independently in both studies. Because independent reconstructions ignore structural information that is inherently correlated across multiple acquisitions (30–32), image quality can be degraded at high acceleration factors that are critically needed with increasing N.

Here we propose an improved framework for accelerating phase-cycled bSSFP imaging that jointly reconstructs undersampled data across multiple acquisitions. Analogous to parallel imaging that takes each coil image as the product of the tissue image with a respective coil sensitivity (33), this framework models each phase-cycled bSSFP image as the product of the banding-artifact-free image with a respective bSSFP spatial profile (34, 35). Thus, inspired by recent approaches for multi-coil imaging (32), the joint reconstruction is cast as a profile-encoding problem (PE-SSFP) where nonacquired k-space samples are linearly synthesized from acquired data. To further alleviate aliasing and noise interference, PE-SSFP leverages joint-sparsity and total-variation penalties. Comprehensive simulations are presented to demonstrate the reliability of PE-SSFP against variations in sequence and tissue parameters, noise, and field inhomogeneity. Phantom and in vivo results clearly indicate that the proposed framework yields improved image quality over conventional reconstructions.

# Methods

The goal of the current study is to implement robust, artifact-free multiple-acquisition bSSFP imaging within a total scan time equivalent to a single acquisition. Starting with an overview of phase-cycled bSSFP imaging, the following sections discuss the sampling and reconstruction strategies proposed towards this goal.

## Multiple-Acquisition Phase-Cycled bSSFP Imaging

In multiple-acquisition bSSFP, several images with different phase-cycling are acquired such that banding artifacts are spatially non-overlapping across acquisitions. Assuming TE=TR/2, the fully-sampled images at each phase cycle can be expressed as (36):

$$S_n(r) = M(r)\frac{e^{i(\phi(r)+\Delta\phi_n)/2}\left(1 - A(r)e^{-i(\phi(r)+\Delta\phi_n)}\right)}{1 - B(r)\cos(\phi(r) + \Delta\phi_n)} \tag{1}$$

where $r$ denotes spatial location, $\phi(r)$ is phase accrued in a single TR due to field inhomogeneity, and $\Delta\phi_n$ is the phase-cycling value used for the $n^{th}$ acquisition where $n \in [1\ \mathrm{N}]$. The remaining terms $M$, $A$, $B$ depend on sequence and tissue parameters. Tailored image combination techniques are then used to minimize the dependence of the bSSFP signal on $\phi(r)$ $(20, 22)$. An artifact-free image $(S_o)$ could be obtained under the condition that $\phi(r) + \Delta\phi_n = \pi$, which in turn would yield:

$$S_o(r) = iM(r)\frac{1 + A(r)}{1 + B(r)} \tag{2}$$

Thus, each phase-cycled image $S_n$ can be modeled as the multiplication of $S_o$ with a respective bSSFP profile, $C_n$ as illustrated in Fig. 1:

$$C_n(r) = \frac{S_n(r)}{S_o(r)} = \frac{e^{i(\phi+\Delta\phi_n-\pi)/2}\,(1 + B)\left(1 - Ae^{-i(\phi+\Delta\phi_n)}\right)}{(1 + A)(1 - B\cos(\phi + \Delta\phi_n))} \tag{3}$$

Combination techniques for multiple-acquisition bSSFP typically assume that data are either fully-sampled (20–22) or else adequately reconstructed (25). Estimation of bSSFP profiles has therefore not been of particular interest, apart from cases where signal-to-noise ratio (SNR) optimization or fat-water separation is aimed (23, 34). Nonetheless, the bSSFP profiles can be interpreted as a means to perform spatial encoding (35), similar to that implemented by the coil sensitivities in parallel imaging (33). With this interpretation, we cast the joint reconstruction of undersampled phase-cycled acquisitions as a profile-encoding problem:

$$y_n(k) = \mathcal{F}_n \{C_n(r) \cdot S_o(r)\} \tag{4}$$

Here $k$ indicates k-space location, $y_n$ are the k-space data for the n$^{th}$ acquisition, and $\mathcal{F}$ is a Fourier-transform operator. For simplicity, we did not consider the effects of coil sensitivities on the joint reconstruction. Thus, assuming that bSSFP spatial profiles can be estimated based on fully-sampled central k-space data (37, 38), they can be used to solve an inverse problem that recovers the artifact-free bSSFP image $S_o(r)$ given a collection of phase-cycled data $y_n(k)$.

## Undersampling Patterns for Multiple-Acquisition bSSFP Data

Each of N separate phase-cycled acquisitions were undersampled by a factor of R=N. Sampling patterns for phase-cycled acquisitions can be selected independently. A common pattern for all acquisitions can better enforce consistency in the sampling matrix across phase-cycles, and reduce interpolation errors. On the other hand, disjoint patterns across acquisitions can expand k-space coverage, and reduce aliasing artifacts (25). To optimize sampling strategy, we compared reconstructions of data undersampled with common versus disjoint patterns. Patterns were generated using uniform-density deterministic (33, 35), variable-density random (28), and Poisson-disc sampling (32). In all cases, isotropic acceleration was performed in two dimensions, and a central k-space region spanning up to 10% of the maximum spatial frequency in each axis was fully sampled. In uniform-density sampling, the full sampling matrix was linearly ordered and then undersampled by holding every N$^{th}$ sample (e.g., 1, N+1,...). Disjoint patterns were generated by incrementing the starting index by 1 sample (35). In variable-density sampling, random patterns were generated based on a polynomial probability density function (PDF), and sampling patterns were selected among 2000 candidate patterns to minimize aliasing energy (39). Disjoint patterns were selected by minimizing both the aliasing energy for each pattern and the pair-wise correlation among patterns (25). In Poisson sampling, a polynomial PDF was used to generate a random sampling pattern that maintains locally-uniform inter-sample distances. Disjoint patterns were generated by using a distinct starting seed for the sampling algorithm (32).

## Profile-Encoding Reconstruction

In a recent study, we proposed to alleviate banding artifacts by combining separate CS reconstructions of individual phase-cycled bSSFP acquisitions (25). The individual-CS reconstruction (iCS) was implemented via a Lagrangian formulation:

$$\min_{m_n} \quad \|y_n - \mathcal{F}_{\mathcal{P}n}\{m_n\}\|_2^2 + \lambda_1 \|\psi\{m_n\}\|_1 + \lambda_2 \|\nabla\{m_n\}\|_1 \tag{5}$$

This formulation comprised a data-consistency term (where $y_n$ is the acquired data, $\mathcal{F}_{\mathcal{P}n}$ is the partial Fourier operator, and $m_n$ is the reconstructed image for the n$^{th}$ phase cycle), a sparsity term (where $\psi$ is a wavelet-transform operator), and a total-variation term (TV; where $\nabla$ is the finite difference operator). While iCS was shown to maintain good reconstruction quality for small N, loss of high-spatial-frequency information became prominent for N≥4 due to increasingly heavier undersampling factors (25).

To address this limitation, we propose a profile-encoding bSSFP (PE-SSFP) reconstruction that solves the problem in Eq. 4 by synthesizing missing k-space samples from acquired data. First, an interpolation operator estimated from calibration data is used to iteratively synthesize nonacquired data across phase-cycles. Inspired by the SPIRiT model (iterative self-consistent parallel imaging) (32), the iterative estimation procedure enforces the consistency of reconstructed data with both the acquired and the calibration data. Lastly, PE-SSFP leverages joint sparsity (30, 31, 40) and TV penalties (28) to dampen aliasing and noise interference. Here PE-SSFP was implemented as a constrained optimization problem:

$$\begin{aligned} \min_{m} \quad & \lambda_1 \left\| \sqrt{\sum_n |\psi\{m_n\}|^2} \right\|_1 + \lambda_2 \sum_n \|\nabla\{m_n\}\|_1 \\ \text{subj. to} \quad & \|(\mathcal{G} - I)\{m\}\|_2^2 = 0 \\ & \sum_n \|y_n - \mathcal{F}_{\mathcal{P}n}\{m_n\}\|_2^2 = 0 \end{aligned} \tag{6}$$

where $m$ is the aggregate vector containing $m_n$ across all phase-cycles. The objective comprises a joint sparsity term and a cumulative TV term across phase cycles. The first constraint enforces consistency of reconstructed data with the calibration data (where $\mathcal{G}$ is the aggregate interpolation operator, $I$ is the identity operator). Meanwhile, the second constraint enforces cumulative data-consistency across phase cycles.

To efficiently solve the constrained optimization formulated in Eq. 6, we leveraged an alternating projection-onto-sets scheme with the aim to produce a quasi-optimal solution at the intersection of multiple sets (40). The optimization was split into four projection operators, namely calibration consistency, joint sparsity, TV, and data consistency projections. These projections were successively repeated to enforce relevant properties in the reconstructed data (see Fig. 2).

*Calibration consistency:* Prior to reconstruction, an interpolation kernel for profile encoding ($\mathcal{K}$) was obtained from aggregate calibration data $y_{calib}$ (designated as the fully-sampled part of central k-space). Kernel weights that capture linear relationships among 11×11 neighborhoods of k-space samples were estimated based on the calibration constraint $(\mathcal{K} - I).y_{calib} = 0$. A 13×13 kernel was used at N=2 to leverage the relatively higher sampling density in central k-space. The solution of this inverse problem was obtained via Tikhonov regularization (with weight $\alpha = 0.01$) to enhance noise resilience and conditioning (40). Finally, an image-space operator $\mathcal{G}$ equivalent to the trained k-space kernel $\mathcal{K}$ was computed. During reconstruction, calibration-consistency projections were implemented by applying $\mathcal{G}$ on the image reconstructed in the previous iteration, $m^{(k)} = \mathcal{G}\left\{m^{(k-1)}\right\}$.

*Joint sparsity:* Assuming insignificant motion between separate acquisitions, tissue boundaries and sparsity patterns are expected to appear in identical locations across phase-cycled images. To leverage this correlated structural information, we utilized a joint-sparsity model that has been shown to offer benefits in other MR applications (30–32, 41, 42). During PE-SSFP, the joint-sparsity term in Eq. 6 based on the Daubechies 4 wavelet can offer increased detection sensitivity for relatively small coefficients shared across phase cycles.

Wavelet-domain sparsity is conventionally enforced via shrinkage methods based on hard- $S_h(x) = \frac{x}{|x|-\lambda}.\max(0, |x|-\lambda)$ or soft-thresholding $S_s(x) = \frac{x}{|x|}.\max(0, |x|-\lambda)$, where $\lambda$ is the threshold (43).

Both functions null wavelet coefficients below $\lambda$, potentially reducing detection sensitivity for small coefficients. To alleviate this issue, here we used a modified Huber function (44) :

$$S_{huber}(x) = \begin{cases} x^2/(2\lambda) & , |x| < \lambda \\ |x| - \lambda/2 & , \text{otherwise} \end{cases} \tag{7}$$

This function behaves similarly to soft-thresholding above $\lambda$, but it applies squared-weighting on small coefficients to increase detection sensitivity. Note that iterative thresholding based on this function provides a quasi-proximal mapping for the $\ell_1$-norm, thus $\lambda$ was set to $\lambda_1$ in Eq. 6. During PE-SSFP, the following joint-sparsity projections were applied: $m^{(\dot{k})} = \psi^{-1}\left\{S_{huber}(\psi\{m^{(k)}\})\right\}$.

*TV:* Total-variation projections were employed to reduce aliasing interference and noise. The projections were implemented by minimizing the objective $J(x) = \|m_n - x\|_2^2 + \lambda_2\|\nabla x\|_1$ using a fast iterative-clipping algorithm:

$$\begin{aligned} x^{(i)} &= m_n^{(\dot{k})} - \nabla^t z^{(i-1)} \\ z^{(i)} &= S_{clip}\left(z^{(i-1)} + \nabla x^{(i)}/\alpha\right) \end{aligned} \tag{8}$$

where $\nabla^t$ is the adjoint finite-difference operator, $z^{(1)} = 0$ and the update rate parameter $\alpha = 8$ (45). The clipping function was modified to handle complex values:

$$S_{clip}(z) = \begin{cases} z & , |z| < \lambda_2/2 \\ (\lambda_2/2) \cdot exp(j\angle(z)) & , \text{otherwise} \end{cases} \tag{9}$$

where $\angle(z)$ is the phase of $z$. This algorithm converges rapidly, and the percentage change in the objective fell to 0.01% within 5 iterations during each TV projection: $m^{(\ddot{k})} = TV_{proj}\left\{m^{(\dot{k})}\right\}$.

*Data consistency:* To ensure consistency of reconstructed and acquired k-space data, reconstructed data were projected onto the constraint $\sum\limits_n \|y_n - \mathcal{F}_{\mathcal{P}n}\{m_n\}\|_2^2 = 0$. This projection was implemented by replacing reconstructed data with the acquired data in sampled locations (40): $m^{(\dddot{k})} = \mathcal{F}^{-1}\left\{(\mathcal{F} - \mathcal{F}_{\mathcal{P}})\{m^{(\ddot{k})}\} + y\right\}$.

The successive projections listed above were repeated until the percentage difference between the reconstructed images in consecutive iterations fell to 0.001%. Convergence was achieved within 15 iterations for the datasets considered here (see Sup. Fig. S1 for typical changes in joint sparsity, TV and cumulative cost terms during PE-SSFP). The total reconstruction times are listed in Sup. Table S1. The penalty weights $\lambda_{1,2}$ were varied separately in the range $[0\ 10] \times 10^{-3}$ with a step size of $10^{-3}$ for phantom data, and in the range $[0\ 15] \times 10^{-3}$ with a step size of $0.05 \times 10^{-3}$ for in vivo data (39). To minimize potential block artifacts and resolution losses, the smallest set of $\lambda_{1,2}$ that yielded satisfactory artifact/noise suppression were selected via visual inspection (see Sup. Table S2). To obtain a final bSSFP image, reconstructions for each phase-cycle were combined with the p-norm method (p=4), which was selected for its computational simplicity and favorable performance in artifact suppression and SNR efficiency (34).

## Alternative Reconstructions

To comparatively demonstrate PE-SSFP, zero-filled Fourier (ZF), individual CS (iCS) and ESPIRiT (46) reconstructions were also implemented. All methods reconstructed individual phase-cycled images that were then p-norm combined (p=4).

*ZF:* Nonacquired k-space data were filled with zeros. Data for each phase-cycle were compensated for the sampling density across k-space. An inverse Fourier transformation was then performed to reconstruct each phase-cycled image.

*iCS:* Individual CS reconstructions of phase-cycled acquisitions were implemented as described in Eq. 5. The sparsifying transform was selected as the Daubechies 4 wavelet. The optimization was performed using an iterative conjugate-gradient algorithm (28). Iterations were repeated until the percentage difference between the reconstructed images in consecutive iterations fell to 0.01%. Convergence was achieved within 30 iterations for the datasets considered here. Further iterations were avoided because they were observed to cause undesirable blurring in the reconstructions. The regularization weights were scaled proportionately to those in PE-SSFP. Specifically, $\lambda_1$ was set to maintain the same ratio of sparsity to data-consistency terms ($\sqrt{N} \times \lambda_{1,PE-SSFP}$), $\lambda_2$ was set to maintain the same ratio of TV to data-consistency terms ($\lambda_{2,PE-SSFP}$).

*ESPIRiT:* A soft-SENSE reconstruction (33) based on multiple sets of bSSFP profiles was implemented using the $\ell_1$-ESPIRiT framework (46). Profile estimates were obtained via eigenvector decomposition of $\mathcal{G}$ in the image domain. Separate sets of profile estimates were obtained for each phase cycle ($\hat{C}_n^j$ for the $j^{th}$ set, $j \in [1\ J]$), by selecting eigenvalues above a fixed threshold of 0.9 with a null-space cut-off $\sigma^2_{\text{cutoff}}$=0.02. This yielded two sets of bSSFP profiles estimates for the datasets reported here. Individual phase-cycled images $m_n$ were then reconstructed via the following optimization:

$$\min_{m} \quad \sum_n \|y_n - \mathcal{F}_{\mathcal{P}_n}\{m_n\}\|_2^2 + \lambda_1 \left\| \sqrt{\sum_n |\psi\{m_n\}|^2} \right\|_1 \tag{10}$$

where $m_n = \sum_j \hat{C}_n^j m_n^j$. Variable splitting with a splitting parameter of 0.4 was implemented to decompose the optimization into two subproblems that minimize the profile-encoding cost (first term in the objective) and the joint-sparsity cost (second term) respectively (47). The profile-encoding subproblem was solved via a conjugate gradient algorithm with 20 iterations (40). Remaining reconstruction parameters including the number of outer iterations were kept identical to PE-SSFP.

## Simulations

Simulations were performed based on a realistic brain phantom at 0.5 mm isotropic resolution (http://www.bic.mni.mcgill.ca/brainweb). Phase-cycled bSSFP signals for each tissue were calculated based on Eq. 1, assuming the following $T_1/T_2$: 3000/1000 ms for cerebro-spinal fluid (CSF), 1200/250 ms for blood, 1000/80 ms for white matter, 1300/110 ms for gray matter, 1400/30 ms for muscle, and 370/130 ms for fat. Meanwhile, three-dimensional (3D) acquisitions were simulated using $\alpha = 45^o$ (flip angle), TR = 5.0 ms, TE = 2.5 ms, 10 axial cross-sections equispaced to cover the whole brain in the superior-inferior direction, and $\Delta\phi = 2\pi\frac{[0:1:(N-1)]}{N}$. The simulations used a realistic field-inhomogeneity distribution corresponding to an off-resonance shift of 0±62 Hz (mean±std; see Fig. 1).

To demonstrate the auto-calibration approach used in PE-SSFP, we examined how well the acquired data can be represented via the bSSFP profiles estimated from calibration data. Using the profiles extracted by the ESPIRiT method (46), each phase-cycled image was projected onto the subspace spanned by the bSSFP profiles. A difference map was then calculated between each image and its projection onto this subspace. An aggregate error map was finally formed via sum-of-squares combination of difference maps across phase cycles. Error maps were generated for varying kernel sizes (5, 7, 9, 11, 13, 15, 17), calibration area sizes (6%, 8%, 10%, 12%, 14% of the maximum spatial frequency), and null-space cut-offs ($\sigma^2_{\text{cutoff}}$=2x$10^{-1,-2,-3,-4,-5}$).

Next, simulated brain images were undersampled by a factor of N in two phase-encode dimensions using patterns generated for uniform-density, variable-density, and Poisson disc sampling. Separate acquisitions were obtained for common and disjoint sampling patterns across phase cycles. PE-SSFP and alternative reconstructions were performed.

Reconstruction quality was assessed by several different metrics measured on combined bSSFP images. For a given cross-section, a mean-squared error (MSE) was first measured between the image reconstructed from N undersampled acquisitions and a reference image Fourier reconstructed from N=8 fully-sampled acquisitions. Because N=8 is typically sufficient for artifact suppression, MSE assessed the reconstruction performance in reducing banding artifacts in addition to aliasing/noise interference. The peak signal-to-noise (PSNR) metric was then derived from this MSE measurement to summarize the overall image quality. Lastly, a mean structural similarity index (SSIM) was measured between the reconstructed image and the reference image for N=8, following histogram matching to account for large-scale intensity variations (25). SSIM assessed the degree of visual similarity in tissue structure to the reference image. To assess the reliability of PE-SSFP against field inhomogeneity, residual banding artifacts were evaluated on combined bSSFP images. CSF, white matter and gray matter signals were segregated via tissue masks. The level of residual artifact for each tissue was then characterized based on a percentage ripple metric. Ripple was taken as the ratio of the range of signal intensity to the mean intensity level. All metrics were pooled across 10 cross-sections in the phantom.

Several variants of PE-SSFP were implemented to assess the relative importance of the individual projection stages of the proposed method: $\text{PE}_{calib}$ with only calibration and data-consistency projections; $\text{PE}_{huber}$ with calibration, sparsity (based on Huber thresholding) and data-consistency projections; $\text{PE}_{soft-TV}$ with calibration, sparsity (based on soft thresholding), TV and data-consistency projections. Each additional projection included in PE-SSFP significantly improved the PSNR and SSIM values ($p<0.005$, signed-rank test; see Sup. Table S3). Furthermore, PE-SSFP outperformed that $\mathrm{PE}_{soft-TV}$ for all N>2 (p<0.005). Thus, Huber thresholding was prescribed for all PE-SSFP reconstructions thereafter.

To examine the effect of tissue and sequence parameters on reconstruction performance, additional simulations were performed based on varying $\mathrm{T}_1/\mathrm{T}_2$ ratios, flip angles, TRs (with TE = TR/2), SNR levels, and acceleration factors (R). The following parameters were considered: (-40%, -20%, 0%, 20%, 40%) deviation in $\mathrm{T}_1/\mathrm{T}_2$ ratios, $\alpha = (15^o, 30^o, 45^o, 60^o, 75^o)$, TR = (5 ms, 10 ms, 15 ms), SNR levels ranging in [10 30] for CSF. To examine performance when R exceeds number of acquisitions (N), the following cases were simulated (N=2, R=4), (N=4, R=6), (N=4, R=8), and (N=6, R=8).

To evaluate noise performance, the SNR levels in the reconstructed images were compared against those in fully-sampled images. For this analysis, 30 separate noise instances with a bivariate Gaussian distribution were added to phase-cycled bSSFP images to attain acquisition SNR=20 for CSF. Each dataset was reconstructed to yield 30 separate combined bSSFP images. The SNR of each voxel was taken as the ratio of the mean to standard deviation of signal intensity across 30 images. A noise amplification map was then computed as the SNR ratio between the fully-sampled reference and reconstructed images. Significance of differences among reconstruction methods were assessed with nonparametric Wilcoxon signed-rank tests.

## In Vivo Experiments

In vivo phase-cycled bSSFP images of the brain and the knee were collected on a 3 T Siemens Magnetom scanner (maximum gradient strength of 45 mT/m and slew rate of 200 T/m/s) with a 3D Cartesian sequence. The brain imaging protocol comprised a flip angle of $30^o$, a TR/TE of 5.1/2.65 ms, a field-of-view (FOV) of 218 mm, an isotropic resolution of 0.85 mm, superior/inferior readout direction, N=8 separate acquisitions with phase-cycling values ($\Delta\phi$) spanning $[0, 2\pi)$ in equispaced intervals, and a 32-channel receive-only head coil. The knee imaging protocol comprised a flip angle of $30^o$, a TR/TE of 5.0/2.5 ms, an FOV of 192 mm, an isotropic resolution of 1 mm, left/right readout direction, N=8, and a 15-channel receive-only knee coil. Fully-sampled images were combined across coils to obtain single-channel multiple acquisition datasets. All participants gave written informed consent, and the imaging protocols were approved by the local ethics committee.

The brain and knee acquisitions were variable-density undersampled in the phase-encode dimensions to yield acceleration factors of 2-8, and profile-encoding reconstructions were performed. The following phase-cycling values were selected for reconstruction: $\Delta\phi = 2\pi\frac{[0:1:(N-1)]}{N}$ for N = 2, 4 and 8. The phase cycles for N = 6 were selected as a subset of those for N =8 (0, $\pi/2$, $3\pi/4$, $\pi$, $5\pi/4$, $7\pi/4$) to reduce overall scan time and minimize potential motion artifacts.

To examine the quality of reconstructed images, PSNR and SSIM metrics were measured across 10 equispaced cross-sections. For brain images, axial cross-sections were used that spanned across the entire volume in the superior-inferior direction. For knee images, sagittal cross-sections in the left-right direction were used. The reference image was taken as the combined Fourier reconstruction of N=8 fully-sampled acquisitions.

# Results

## Simulation Analyses

PE-SSFP was first demonstrated on bSSFP images of a numerical brain phantom. Figure 3 shows the combination bSSFP images reconstructed via ZF, iCS and PE-SSFP. As expected, heavier undersampling applied at higher N values increases aliasing interference in ZF images. Meanwhile iCS reconstructions, which process phase cycles independently, suffer from prominent losses in spatial resolution. In contrast, PE-SSFP successfully reduces aliasing interference while maintaining detailed tissue depiction even at N = 8.

Several complementary analyses were performed to elucidate factors contributing to reconstruction performance. To demonstrate the auto-calibration approach in PE-SSFP, errors were examined in representing acquired data in terms of the bSSFP profiles estimated from calibration data (Sup. Figs. S2 and S3). For the kernel size, calibration area and null-space cutoff prescribed in PE-SSFP, residual high-spatial-frequency errors occur near banding artifacts for each phase cycle. When combined across phase-cycles, the auto-calibration errors appear near tissue boundaries rather uniformly across the FOV. The average auto-calibration error relative to the maximum signal intensity is 3.2±0.6% (mean±s.e. across N). The percentage improvement that can be attained by advancing the kernel size, calibration area or null-space cutoff to their optimal values in the tested range is merely 1.0±0.3%. Thus, the selected PE-SSFP parameters yield near-optimal results with relatively low error levels. To determine the effects of individual projection operators in PE-SSFP, several variant reconstructions and respective squared-error maps relative to a fully-sampled image were computed (Fig. 4). The inclusion of each projection visibly reduces error across the image. To examine noise statistics of the reconstructions, noise amplification factors were calculated across the images (Fig. 5). Although the heavier undersampling at high N increases noise in ZF, penalty terms in iCS and PE-SSFP help maintain lower noise. In PE-SSFP, relatively higher amplification is observed near tissue boundaries that are more susceptible to resolution loss due to variable-density undersampling.

**R2.1**: Text revised

To determine the effect of the sampling strategy on PE-SSFP, uniform-density, variable-density and

Poisson disc undersampling patterns were tested. Each type of pattern was applied both commonly and disjointly across phase cycles. While all sampling strategies yield similar PSNR and SSIM values at N=2 (Sup. Table S4), variable-density (VD) disjoint sampling outperforms all other methods for N>2 ($p<0.005$). VD disjoint sampling improves PSNR by 4.0±1.9 dB (mean±s.e. across N) and SSIM by 0.8±0.5% over VD common sampling, and PSNR by 3.2±1.6 dB and SSIM by 0.4±0.2% over Poisson-disc disjoint sampling. Thus VD disjoint sampling was used for all reconstructions reported here.

Finally, PE-SSFP was comparatively evaluated against ZF, iCS and ESPIRiT. Representative images for N=8 are shown in Fig. 6 along with the squared-error maps in reference to a fully-sampled image. While ZF shows broadly distributed errors across the field-of-view, iCS reduces noise and aliasing interference at the expense of losses in high-spatial-frequency information. While ESPIRiT reconstructions alleviate this loss via joint-sparsity penalties, the respective images still show distributed errors. In contrast, PE-SSFP using both joint-sparsity and TV regularization effectively dampens the reconstruction errors in phase-cycled bSSFP images.

The observations regarding PE-SSFP's superior image quality are supported by the quantitative assessments listed in Table 1. For each N, PE-SSFP yields significantly higher PSNR and SSIM values compared to all other reconstructions ($p<0.005$), with the exception of N=2 where iCS and PE-SSFP yield similar values. PE-SSFP improves PSNR by 13.1±5.0 dB and SSIM by 4.8±2.5% over iCS, and PSNR by 14.5±3.2 dB and SSIM by 3.4±0.6% over ESPIRiT. Extended simulations presented in Sup. Tables S5 and S6 indicate that these results are valid ($p<0.005$) broadly across varying flip angles ($15^o$-$75^o$), $T_1/T_2$ ratios (-40% to 40%), TRs (5-15 ms), noise levels (SNR=10-30), and when the acceleration factor exceeds N. The percentage ripple measurements listed in Table 1 indicate that PE-SSFP yields more homogeneous tissue signals compared to alternative methods for all N ($p<0.005$). Taken together, these results suggest that PE-SSFP reliably enhances image quality and artifact suppression compared to conventional reconstructions.

### In Vivo Analyses

PE-SSFP was demonstrated on bSSFP acquisitions of the brain and the knee. Similar to phantom results, the auto-calibration error was relatively low with 6.1±1.3% error (mean±s.e. across N) in the brain, and 3.7±0.7% error in the knee. Figure 7 shows the combined PE-SSFP images and the squared-error maps for N=2-8. As expected, prominent errors due to residual banding are visible for lower N values. These errors are alleviated towards high N, while maintaining high-quality tissue depiction. Representative images from ZF, iCS, ESPIRiT and PE-SSFP are displayed in Fig. 8. While iCS incurs losses at high spatial frequencies and coherent interference at low frequencies, ESPIRiT suffers from broadly distributed reconstruction errors across the images. In contrast, PE-SSFP visibly reduces reconstruction errors and preserves high-spatial-frequency information.

Quantitative assessments of in vivo reconstructions are listed in Table 2. In both the brain and the knee, PE-SSFP yields significantly higher PSNR and SSIM values compared to iCS for $N>2$ ($p<0.05$). PE-SSFP also improves PSNR and SSIM compared to all other alternative reconstructions for all N ($p<0.05$), with the exception of knee images at N=8 where PE-SSFP and ESPIRiT yield similar PSNR. In the brain, PE-SSFP improves PSNR by 3.0±2.6 dB and SSIM by 1.4±1.2% over iCS, and PSNR by 8.5±0.8 dB and SSIM by 7.1±0.5% over ESPIRiT. In the knee, PE-SSFP improves PSNR by 4.7±3.5 dB and SSIM by 1.8±0.6% over iCS, and PSNR by 2.8±1.2 dB and SSIM by 8.3±0.4% over ESPIRiT. Taken together, these results strongly suggest that the proposed method enables scan-efficient suppression of banding artifacts at high N values, while maintaining detailed tissue structure via the joint reconstruction.

## Discussion

Here we evaluted an improved acceleration framework for multiple-acquisition 3D bSSFP based on variable-density random undersampling in two phase-encode dimensions. In this framework, nonacquired data across phase-cycles are simultaneously synthesized using a profile-encoding reconstruction that enforces joint sparsity and TV penalties. A p-norm combination of individual phase-cycled images yields a final artifact-suppressed bSSFP image.

Several alternative approaches were previously proposed for reducing banding artifacts. One strategy is to increase the tolerable range of field inhomogeneity by modifying the bSSFP magnetization profile (12–15). Alternatively, advanced shimming procedures can be performed to directly limit field inhomogeneity (16). While both strategies aim to reduce banding artifacts during acquisition, they require complex pulse-sequence modifications and prolonged scan times. In contrast, our proposed framework can be implemented via standard bSSFP sequences without separate calibration procedures.

Improvements in scan efficiency of multiple-acquisition bSSFP have been considered in several previous reports. Recently, we proposed to undersample and individually reconstruct phase-cycled acquisitions using CS (25). The CS framework yielded high quality reconstructions up to an acceleration factor of N=4. Another study employed simultaneous multislice imaging to accelerate each acquisition separately, and similarly considered $N \leq 4$ (26). While these previous studies disregarded image features shared across phase-cycles, here we used a joint-sparsity model to enhance recovery of wavelet coefficients, and TV regularization to reduce aliasing and noise interference. Due to these advances, PE-SSFP maintains high-quality reconstructions up to N=8. Spatial encoding by coil arrays was not leveraged in the reconstructions reported here. However, if more effective artifact suppression is needed (e.g., while imaging at 7T or near air-tissue interfaces), a higher N value and a respectively higher acceleration factor might be maintained by also leveraging coil sensitivity information. Note, however, that each phase-cycled acquisition involves a fixed-duration overhead due to the preparatory RF pulses employed to reach steady state. This overhead will become more prominent for larger N values, reducing the overall scan efficiency.

With similar motivations to PE-SSFP, one earlier study proposed a SENSE-type reconstruction performed jointly across phase-cycled acquisitions, each accelerated via uniform-density undersampling (35). Sensitivity estimates were taken as the ratio of low resolution phase-cycled images to a maximum-intensity combination of these images. In contrast, here we used variable-density sampling, and we did not assume any combination model while calibrating the interpolation kernel. Our results clearly indicate that variable-density sampling offers improved performance compared to uniform sampling.

PE-SSFP can be potentially improved by addressing several limitations. First, if significant motion occurs in between separate acquisitions, image structure can be displaced across phase-cycles. These displacements may in turn violate the joint-sparsity model and yield suboptimal reconstructions. A motion-correction operator could be incorporated to alleviate motion-induced performance loss. Second, the auto-calibration approach in PE-SSFP relies on the assumption that bSSFP spatial profiles vary gradually. Rapid profile variations near tissue boundaries or bSSFP nulls can yield suboptimal interpolation operators, increasing reconstruction errors. This issue may be of particular concern with high field strengths, long TRs, and certain combinations of $T_1/T_2$ and flip angles. In such cases, the k-space calibration area could be expanded and interpolation kernels of variable widths across k-space could be used to improve accuracy of the interpolation operator (48, 49). Third, while a p-norm combination was observed to yield good artifact suppression in this study, it could be replaced with sophisticated techniques that leverage analytical signal models to further improve artifact suppression (17, 18). Lastly, optimization with the projection-onto-sets method does not guarantee convergence onto a fixed solution in the absence of overlap between the projection sets. While we observed good convergence behavior here, reconstruction stability can be improved by modern approaches such as the alternating direction method of multipliers (50).

In conclusion, the proposed PE-SSFP framework jointly reconstructs multiple-acquisition bSSFP data by leveraging shared sparsity patterns across phase-cycles. PE-SSFP was primarily demonstrated for brain and knee imaging in the current study. Nonetheless, the scan-efficient acquisitions and high-quality reconstructions enabled by PE-SSFP could improve other multiple-acquisition bSSFP applications such as peripheral angiography (51), coronary imaging (52), and fat/water separation (23, 53).

## Acknowledgment

The authors thank A. Emek for his contributions to the initial implementation of this work, and E.U. Saritas for helpful discussions regarding the manuscript. The authors also thank the reviewers for their insightful suggestions that significantly improved the manuscript.

# References

[1] Scheffler K, Lehnhardt S. Principles and applications of balanced SSFP techniques. Eur Radiol 2003; 13:2409–2418.

[2] Peters DC, Ennis DB, McVeigh ER. High-resolution MRI of cardiac function with projection reconstruction and steady-state free precession. Magn Reson Med 2002; 48:82–88.

[3] Bieri O, Patil S, Quick HH, Scheffler K. Morphing steady-state free precession. Magn Reson Med 2007; 58:1242–1248.

[4] Koktzoglou I, Li D, Dharmakumar R. Dephased FLAPS for improved visualization of susceptibility-shifted passive devices for real-time interventional MRI. Phys Med Biol 2007; 52:277–286.

[5] Scheffler K, Seifritz E, Bilecen D, Venkatesan R, Hennig J, Deimling M, Haacke EM. Detection of BOLD changes by means of a frequency-sensitive trueFISP technique: preliminary results. NMR Biomed 2001; 14:490–496.

[6] Miller KL, Hargreaves BA, Lee J, Ress D, de Charms RC, Pauly JM. Functional brain imaging using a blood oxygenation sensitive steady-state. Magn Reson Med 2003; 50:675–683.

[7] Hargreaves BA, Gold GE, Beaulieu CF, Vasanawala SS, Nishimura DG, Pauly JM. Comparison of new methods for magnetic resonance imaging of articular cartilage. Magn Reson Med 2003; 49:700–709.

[8] Vasanawala SS, Hargreaves BA, Pauly JM, Nishimura DG, Beaulieu CF, Gold GE. Rapid musculoskeletal MRI with phase-sensitive steady-state free precession: Comparison with routine knee MRI. AJR Am J Roentgenol 2004; 184:1450–1455.

[9] Çukur T, Nishimura DG. Multiple repetition time balanced steady-state free precession imaging. Magn Reson Med 2009; 62:193–204.

[10] Heyn C, Bowen CV, Rutt BK, Foster PJ. Detection threshold of single SPIO-labeled cells with FIESTA. Magn Reson Med 2005; 53:312–320.

[11] Çukur T, Shimakawa A, Yu H, Hargreaves BA, Hu BS, Nishimura DG, Brittain JH. Magnetization-prepared IDEAL bSSFP: A flow-independent technique for noncontrast-enhanced peripheral angiography. J Magn Reson Imaging 2011; 33:931–939.

[12] Nayak KS, Lee HL, Hargreaves BA, Hu BS. Wideband SSFP: Alternating repetition time balanced steady state free precession with increased band spacing. Magn Reson Med 2007; 58:931–938.

[13] Hargreaves BA. Partially dephased SSFP for elimination of dark bands. In: Proceedings of the 16th Annual Meeting of ISMRM, Toronto, 2008. p. 1357.

[14] Benkert T, Ehses P, Blaimer M, Jakob PM, Breuer FA. Dynamically phase-cycled radial balanced SSFP imaging for efficient banding removal. Magn Reson Med 2015; 73:182–194.

[15] Sun H, Fessler JA, Noll DC, Nielsen JF. Balanced SSFP-like steady-state imaging using small-tip fast recovery with a spectral prewinding pulse. Magn Reson Med 2016; 75:839–844.

[16] Lee J, Lustig M, Kim DH, Pauly JM. Improved shim method based on the minimization of the maximum off-resonance frequency for balanced steady-state free precession (bSSFP). Magn Reson Med 2009; 61:1500–1506.

[17] Xiang QS, Hoff MN. Banding artifact removal for bSSFP imaging with an elliptical signal model. Magn Reson Med 2014; 71:927–933.

[18] Björk M, Ingle RR, Gudmundson E, Stoica P, Nishimura DG, Barral JK. Parameter estimation approach to banding artifact reduction in balanced steady-state free precession. Magn Reson Med 2014; 72:880–892.

[19] Haacke EM, Wielopolski PA, Tkach JA, Modic MT. Steady-state free precession imaging in the presence of motion: Application for improved visualization of the cerebrospinal fluid. Radiology 1990; 175:545–552.

[20] Bangerter NK, Hargreaves BA, Vasanawala SS, Pauly JM, Gold GE, Nishimura DG. Analysis of multiple-acquisition SSFP. Magn Reson Med 2004; 51:1038–1047.

[21] Elliott AM, Bernstein MA, Ward HA, Lane J, Witte RJ. Nonlinear averaging reconstruction method for phase-cycle SSFP. Magn Reson Imaging 2007; 25:359–364.

[22] Çukur T, Bangerter NK, Nishimura DG. Enhanced spectral shaping in steady-state free precession imaging. Magn Reson Med 2007; 58:1216–1223.

[23] Quist B, Hargreaves BA, Çukur T, Morrell GR, Gold GE, Bangerter NK. Simultaneous fat suppression and band reduction with large-angle multiple-acquisition balanced steady-state free precession. Magn Reson Med 2012; 67:1004–1012.

[24] Quist B, Hargreaves BA, Daniel BL, Saranathan M. Balanced SSFP Dixon imaging with banding-artifact reduction at 3 Tesla. Magn Reson Med 2015; 74:706–715.

[25] Cukur T. Accelerated Phase-Cycled SSFP Imaging With Compressed Sensing. Medical Imaging, IEEE Transactions on 2015; 34:107–115.

[26] Wang Y, Shao X, Martin T, Moeller S, Yacoub E, Wang DJJ. Phase-cycled simultaneous multislice balanced SSFP imaging with CAIPIRINHA for efficient banding reduction; doi:10.1002/mrm.26076. Magn Reson Med 2015; 0:0–0.

[27] Block KT, Uecker M, Frahm J. Undersampled radial MRI with multiple coils: Iterative image reconstruction using a total variation constraint. Magn Reson Med 2007; 57:1086–1098.

[28] Lustig M, Donoho D, Pauly JM. Sparse MRI: The application of compressed sensing for rapid MR imaging. Magn Reson Med 2007; 58:1182–1195.

[29] Çukur T, Lustig M, Nishimura DG. Improving non-contrast-enhanced steady-state free precession angiography with compressed sensing. Magn Reson Med 2009; 61:1122–1131.

[30] Liang D, Liu B, Wang J, Ying L. Accelerating SENSE using compressed sensing. Magn Reson Med 2009; 62:1574–1584.

[31] Otazo R, Kim D, Axel L, Sodickson DK. Combination of compressed sensing and parallel imaging for highly accelerated first-pass cardiac perfusion MRI. Magn Reson Med 2010; 64:767–776.

[32] Lustig M, Pauly JM. SPIRiT: Iterative self-consistent parallel imaging reconstruction from arbitrary k-space. Magn Reson Med 2010; 64:457–471.

[33] Pruessmann KP, Weiger M, Scheidegger MB, Boesiger P. SENSE: Sensitivity encoding for fast MRI. Magn Reson Med 1999; 42:952–962.

[34] Çukur T, Lustig M, Nishimura DG. Multiple-profile homogenous image combination: Application to phase-cycled SSFP and multi-coil imaging. Magn Reson Med 2008; 60:732–738.

[35] Lustig M, Santos JM, Pauly JM. A super-FOV method for rapid SSFP banding artifact reduction. In: Proceedings of the 13th Annual Meeting of ISMRM, Miami Beach, 2005. p. 504.

[36] Lauzon ML, Frayne R. Analytical characterization of RF phase-cycled balanced steady-state free precession. Concepts Magn. Reson. 2009; 34A:133–143.

[37] Ying L, Sheng J. Joint image reconstruction and sensitivity estimation in SENSE (JSENSE). Magn Reson Med 2007; 57:1196–1202.

[38] Uecker M, Hohage T, Block KT, Frahm J. Image reconstruction by regularized nonlinear inversion–joint estimation of coil sensitivities and image content. Magn Reson Med 2008; 60:674–682.

[39] Çukur T, Lustig M, Saritas EU, Nishimura DG. Signal Compensation and Compressed Sensing for Magnetization-Prepared MR Angiography. IEEE Trans Med Imaging 2011; 34:107–115.

[40] Murphy M, Alley M, Demmel J, Keutzer K, Vasanawala S, Lustig M. Fast $\ell_1$-SPIRiT compressed sensing parallel imaging MRI: scalable parallel implementation and clinically feasible runtime. IEEE Trans Med Imaging 2012; 31:1250–1262.

[41] Akçakaya M, Hu P, Chuang ML, Hauser TH, Ngo LH, Manning WJ, Tarokh V, Nezafat R. Accelerated noncontrast-enhanced pulmonary vein MRA with distributed compressed sensing. J Magn Reson Imaging 2011; 33:1248–1255.

[42] Doneva M, Börnert P, Eggers H, Stehning C, Sénégas J, Mertins A. Compressed sensing reconstruction for magnetic resonance parameter mapping. Magn Reson Med 2010; 64:1114–1120.

[43] Donoho DL, Johnstone JM. Ideal spatial adaptation by wavelet shrinkage. Biometrika 1994; 81:425–455.

[44] Yu DF, Fessler JA. Edge-preserving tomographic reconstruction with nonlocal regularization. IEEE Trans Med Imaging 2002; 21:159–173.

[45] Chambolle A. Total Variation Minimization and a Class of Binary MRF Models. *in* “Lecture Notes in Computer Science” (Rangarajan A, Vemuri B, Yuille A, Eds.), pp. 136–152–152. Springer Berlin Heidelberg, Berlin, Heidelberg, 2005.

[46] Uecker M, Lai P, Murphy MJ, Virtue P, Elad M, Pauly JM, Vasanawala SS, Lustig M. ESPIRiT–an eigenvalue approach to autocalibrating parallel MRI: where SENSE meets GRAPPA. Magn Reson Med 2014; 71:990–1001.

[47] Huang F, Chen Y, Yin W, Lin W, Ye X, Guo W, Reykowski A. A rapid and robust numerical algorithm for sensitivity encoding with sparsity constraints: self-feeding sparse SENSE. Magn Reson Med 2010; 64:1078–1088.

[48] Cukur T, Santos JM, Nishimura DG, Pauly JM. Varying kernel-extent gridding reconstruction for undersampled variable-density spirals. Magn Reson Med 2008; 59:196–201.

[49] Çukur T, Santos JM, Pauly JM, Nishimura DG. Variable-density parallel imaging with partially localized coil sensitivities. IEEE Trans Med Imaging 2010; 29:1173–1181.

[50] Boyd S, Parikh N, Chu E, Peleato B, Eckstein J. Distributed Optimization and Statistical Learning via the Alternating Direction Method of Multipliers. Found. Trends Mach. Learn. 2011; 3:1–122.

[51] Çukur T, Lee JH, Bangerter NK, Hargreaves BA, Nishimura DG. Non-contrast-enhanced flow-independent peripheral MR angiography with balanced SSFP. Magn Reson Med 2009; 61:1533–1539.

[52] Nayak KS, Hargreaves BA, Hu BS, Nishimura DG, Pauly JM, Meyer CH. Spiral balanced SSFP cardiac imaging. Magn Reson Med 2005; 53:1468–1473.

[53] Çukur T, Nishimura DG. Fat-water separation with alternating repetition time balanced SSFP. Magn Reson Med 2008; 60:479–484.

# List of Tables

Table 1: Image Assessments for the Brain Phantom

**Peak SNR and Structural Similarity**

| | | **N = 2** | **N = 4** | **N = 6** | **N = 8** |
|---|---|---|---|---|---|
| **ZF** | PSNR | 51.8±0.1 | 50.0±0.2 | 47.2±0.1 | 45.9±0.1 |
| | SSIM | 72.8±0.6 | 65.4±0.8 | 62.4±0.8 | 61.2±0.8 |
| **iCS** | PSNR | 57.5±0.5 | 61.3±0.3 | 52.3±0.4 | 49.0±0.3 |
| | SSIM | 97.9±0.1 | 97.0±0.0 | 91.4±0.3 | 88.2±0.3 |
| **ESPIRiT** | PSNR | 48.0±0.1 | 56.3±0.1 | 56.1±0.3 | 54.1±0.3 |
| | SSIM | 93.5±0.1 | 95.8±0.1 | 95.6±0.1 | 95.1±0.1 |
| **PE-SSFP** | PSNR | 57.9±0.4 | 78.2±0.3 | 71.5±0.4 | 64.9±0.3 |
| | SSIM | 98.4±0.1 | 98.8±0.0 | 98.4±0.0 | 98.0±0.0 |

**Percentage Ripple**

| | | **N=2** | **N=4** | **N=6** | **N=8** |
|---|---|---|---|---|---|
| **ZF** | CSF | 38.8±2.1 | 29.7±1.6 | 31.9±2.1 | 32.5±2.1 |
| | White | 72.9±4.0 | 94.7±6.4 | 94.0±5.3 | 97.2±6.5 |
| | Gray | 53.8±2.1 | 73.2±5.1 | 76.3±3.2 | 77.8±5.5 |
| **iCS** | CSF | 23.2±0.8 | 8.9±1.1 | 17.9±1.4 | 23.9±2.6 |
| | White | 8.5±1.1 | 21.4±3.0 | 40.9±5.9 | 48.8±4.3 |
| | Gray | 9.7±1.1 | 17.7±1.4 | 30.8±4.6 | 36.7±6.2 |
| **ESPIRiT** | CSF | 43.9±1.1 | 17.5±2.1 | 18.8±1.5 | 19.7±1.4 |
| | White | 43.7±5.8 | 41.3±7.9 | 47.2±6.3 | 51.4±8.7 |
| | Gray | 39.0±3.8 | 28.7±2.7 | 34.5±3.8 | 36.1±5.0 |
| **PE-SSFP** | CSF | 22.5±0.2 | 2.1±0.2 | 3.4±0.5 | 3.1±0.5 |
| | White | 5.4±0.4 | 5.9±0.5 | 6.3±0.7 | 6.6±0.7 |
| | Gray | 8.3±0.3 | 6.9±0.4 | 6.8±0.4 | 7.4±1.1 |

Image assessment metrics measured in reconstructed bSSFP images of the numerical brain phantom. Metrics are reported separately for each reconstruction method as mean±std across 10 cross-sections. The top panel lists the peak SNR (PSNR) and structural similarity (SSIM) measurements obtained for $\alpha = 45^o$, TR = 5 ms, fixed $T_1/T_2$ values, and a realistic off-resonance frequency map (0±62 Hz). The bottom panel lists the percentage ripple measurements for CSF, white matter and gray matter separately.

Table 2: Image Assessments for In Vivo Datasets

**Brain Images**

| | | **N=2** | **N=4** | **N=6** | **N=8** |
|---|---|---|---|---|---|
| **ZF** | PSNR | 48.6±0.2 | 44.1±0.4 | 41.4±0.4 | 40.3±0.4 |
| | SSIM | 73.5±0.6 | 56.4±0.8 | 50.6±0.7 | 48.9±0.8 |
| **iCS** | PSNR | 58.4±1.0 | 60.7±0.4 | 56.8±0.9 | 53.2±0.9 |
| | SSIM | 93.0±1.0 | 93.2±0.8 | 91.2±0.8 | 88.9±0.9 |
| **ESPIRiT** | PSNR | 49.5±0.5 | 53.4±0.4 | 51.8±0.6 | 52.5±0.5 |
| | SSIM | 84.2±0.7 | 87.6±0.8 | 84.7±0.5 | 86.7±0.7 |
| **PE-SSFP** | PSNR | 56.0±0.7 | 62.5±0.5 | 61.0±0.8 | 61.5±0.7 |
| | SSIM | 92.0±0.5 | 94.0±0.4 | 92.7±0.4 | 93.0±0.3 |

**Knee Images**

| | | **N = 2** | **N = 4** | **N = 6** | **N = 8** |
|---|---|---|---|---|---|
| **ZF** | PSNR | 59.6±0.3 | 57.8±0.5 | 55.7±0.3 | 54.4±0.4 |
| | SSIM | 86.2±0.6 | 77.2±0.9 | 72.8±1.1 | 69.2±1.1 |
| **iCS** | PSNR | 65.2±0.7 | 72.8±0.4 | 65.3±0.9 | 63.0±1.2 |
| | SSIM | 94.7±0.5 | 95.5±0.4 | 92.0±0.4 | 90.5±0.2 |
| **ESPIRiT** | PSNR | 60.5±0.4 | 68.3±0.4 | 70.7±0.6 | 74.6±0.6 |
| | SSIM | 84.5±1.2 | 87.2±2.4 | 87.2±2.4 | 87.8±2.3 |
| **PE-SSFP** | PSNR | 63.9±0.5 | 73.3±0.4 | 73.4±0.7 | 74.5±0.6 |
| | SSIM | 93.5±0.4 | 95.8±0.2 | 95.2±0.3 | 95.4±0.3 |

Image assessment metrics measured in reconstructed bSSFP images of in vivo brain and knee data. Metrics are reported separately for each reconstruction method as mean±std across 10 cross-sections. The top panel lists PSNR and SSIM measurements for brain images, and the bottom panel lists the measurements for knee images.

# List of Figures

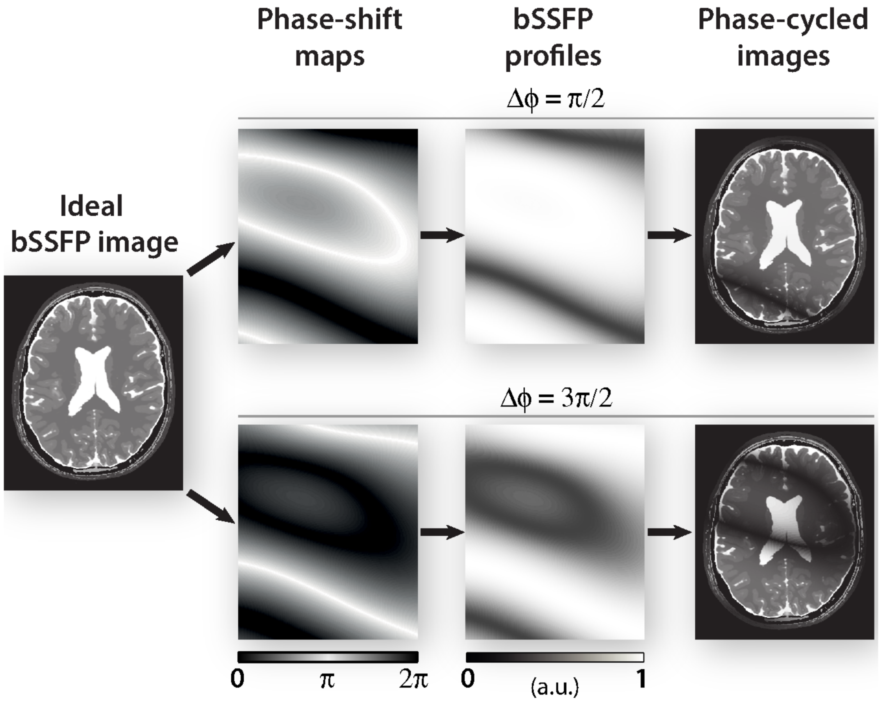

Figure 1: In the profile-encoding framework, each phase-cycled bSSFP image ($S_n$) is modeled as the multiplication of an ideal image free of banding artifacts ($S_o$) with a respective bSSFP sensitivity profile ($C_n$). The value of the bSSFP profile at each location is a function of total phase accrual over a single TR due to main field inhomogeneity and RF phase-cycling increment ($\Delta\phi$). Locations of near-zero phase shift (modulo $2\pi$) lead to significantly diminished sensitivity and thereby banding artifacts in bSSFP images.

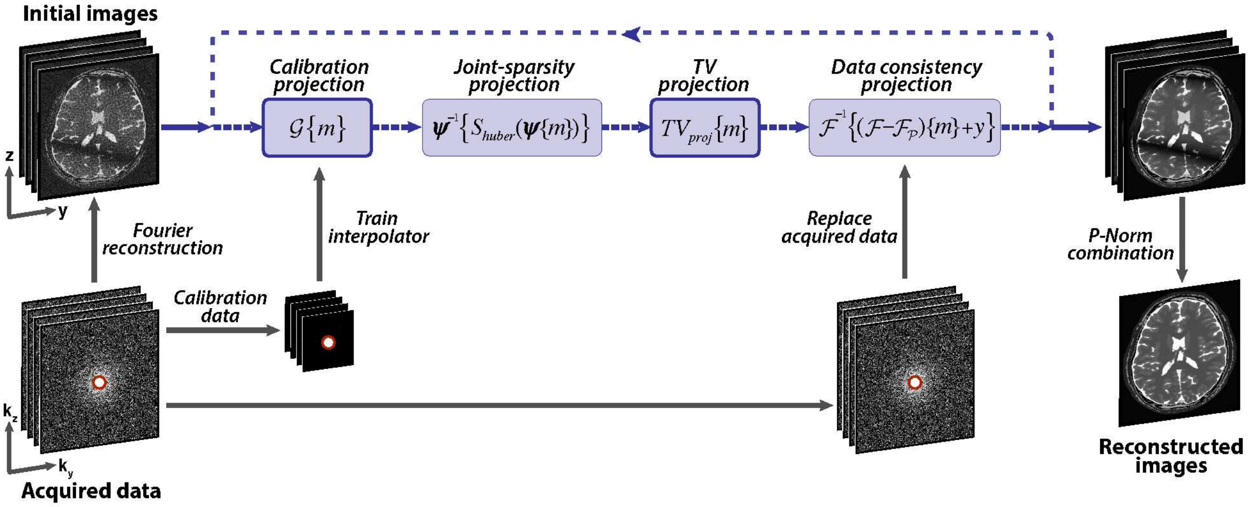

Figure 2: Flowchart of the profile-encoding bSSFP (PE-SSFP) reconstruction that recovers missing data in undersampled phase-cycled acquisitions. PE-SSFP employs an alternating projection-onto-sets scheme with four projection operators: calibration, joint-sparsity, TV, and data-consistency projections. In the calibration projection, an interpolation kernel estimated from calibration data is used to synthesize missing samples linearly from acquired data across phase-cycles. In the joint-sparsity projection, wavelet coefficients of phase-cycled bSSFP images are thresholded with a Huber function. In the TV projection, bSSFP images are denoised with a fast iterative-clipping algorithm. In the data-consistency projection, reconstructed data in sampled locations are replaced with their acquired values. These projections are successively repeated, and the individual phase-cycled images are finally combined with the p-norm method.

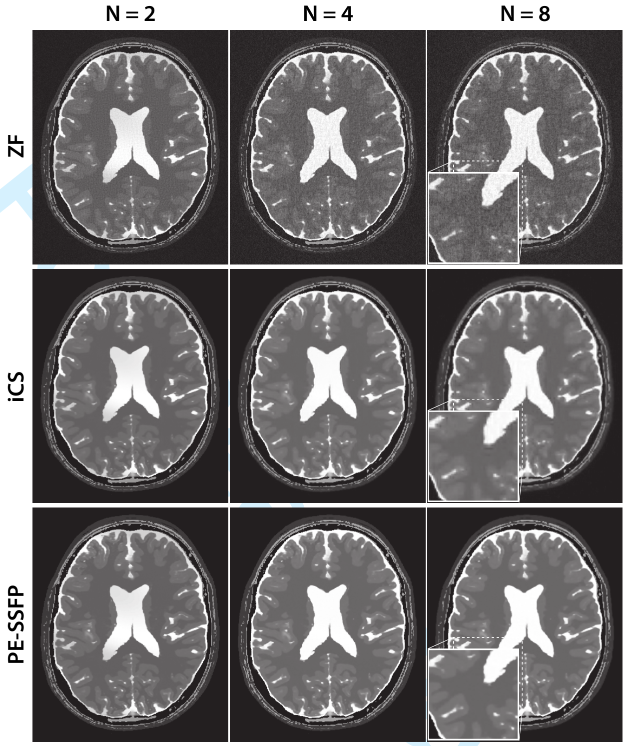

Figure 3: Phase-cycled bSSFP images of a numerical phantom were simulated for N=2-8, $\alpha = 45^o$, TR/TE=5.0/2.5 ms, a field map of 0±62 Hz (mean±std). Phantom images were undersampled by a factor of N via variable-density random sampling, disjointly across phase cycles. Zero-filled Fourier (ZF, top row), individual compressed sensing (iCS, middle row), and PE-SSFP (bottom row) reconstructions are shown. White boxes display a zoomed-in portion of the images. ZF reconstructions suffer from elevated aliasing/noise interference at high N due to the heavier undersampling factors used. While iCS reconstructions employ regularization terms that limit this interference, the heavy undersampling factors at high N cause visible loss of spatial resolution. In contrast, PE-SSFP successfully alleviates noise and aliasing interference while maintaining detailed depiction of tissue boundaries.

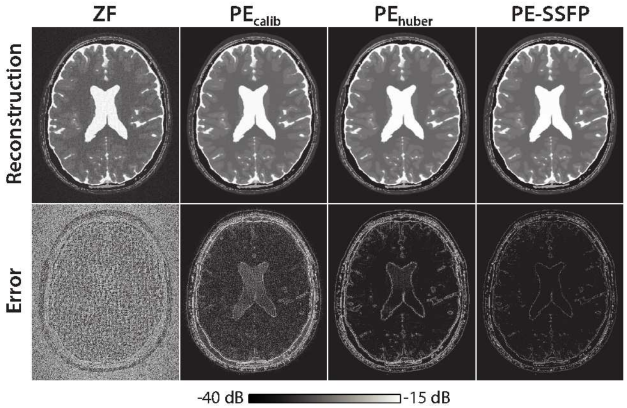

Figure 4: Representative bSSFP images of the numerical phantom for N=4 were reconstructed using ZF and PE-SSFP. Images from three variants of PE-SSFP are shown (top row). $\mathrm{PE}_{calib}$ only uses calibration and data-consistency projections, $\mathrm{PE}_{huber}$ uses calibration, joint-sparsity and data-consistency projections, and PE-SSFP additionally uses TV projections. Reconstructions were compared against a combination of fully-sampled images (for N=8). Squared-error maps are shown in logarithmic scale (bottom row; see colorbar). Each additional projection in PE-SSFP yields visibly reduced reconstruction error in bSSFP images.

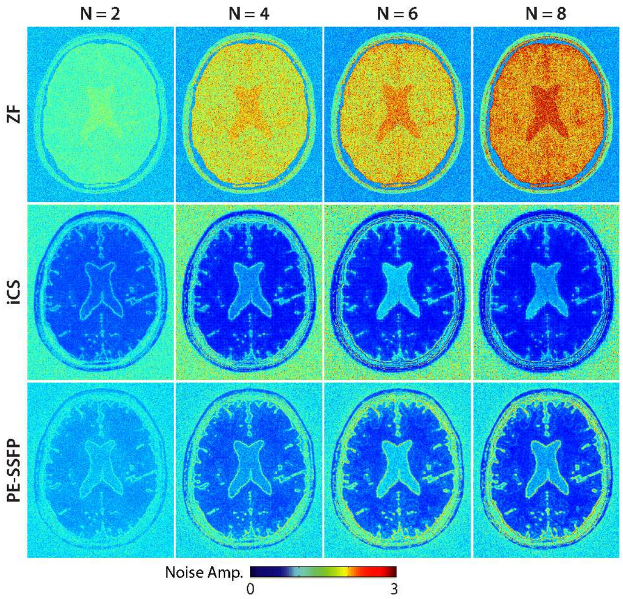

Figure 5: The noise-amplification maps for ZF, iCS and PE-SSFP methods are displayed for N=2-8. Although the heavier undersampling at high N increases noise amplification in ZF reconstructions, reconstructions with penalty terms iCS and PE-SSFP maintain relatively low noise amplification even at high N. The lower noise amplification with iCS likely reflects a bias from excessive loss of high-spatial-frequency information. In PE-SSFP, relatively higher amplification is observed near tissue boundaries that are more susceptible to resolution loss due to variable-density undersampling.

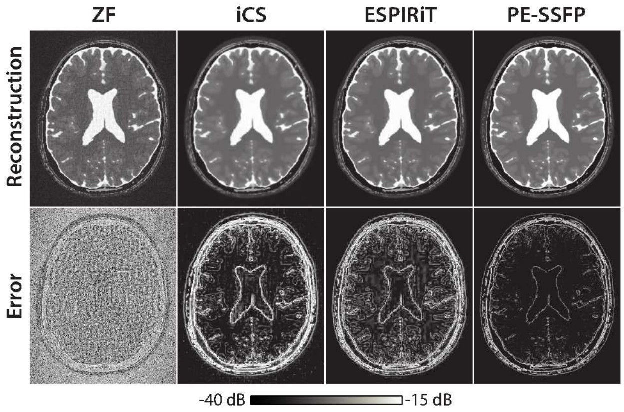

Figure 6: Phase-cycled bSSFP reconstructions of the numerical phantom (top row), and the squared-error maps with respect to the fully-sampled combination image (bottom row) are displayed for N=8. ZF has broadly distributed errors across the field-of-view due to aliasing and noise interference. iCS reconstructions reduce this interference via TV regularization at the expense of elevated errors near tissue boundaries, due to significant loss of high-spatial-frequency information. While ESPIRiT reconstructions alleviate this loss via joint-sparsity penalties, the respective images still show broadly distributed errors. In contrast, PE-SSFP using both joint-sparsity and TV regularization further dampens the reconstruction errors in phase-cycled bSSFP images.

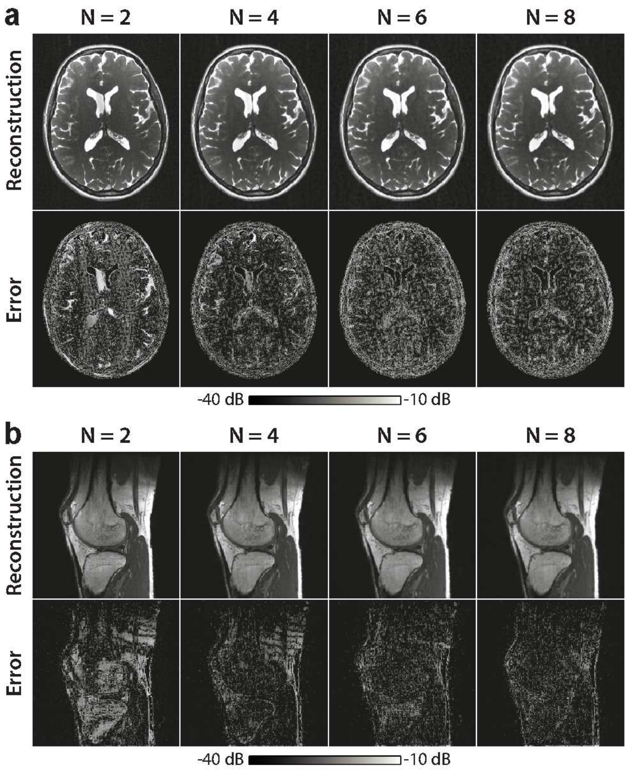

Figure 7: In vivo bSSFP acquisitions of the brain **(a)** and the knee **(b)** were reconstructed using PE-SSFP. Squared-error maps are shown in logarithmic scale (see colorbar). The error maps clearly suggest that banding artifact suppression improves for higher N, while PE-SSFP maintains detailed depiction of high-spatial-frequency information.

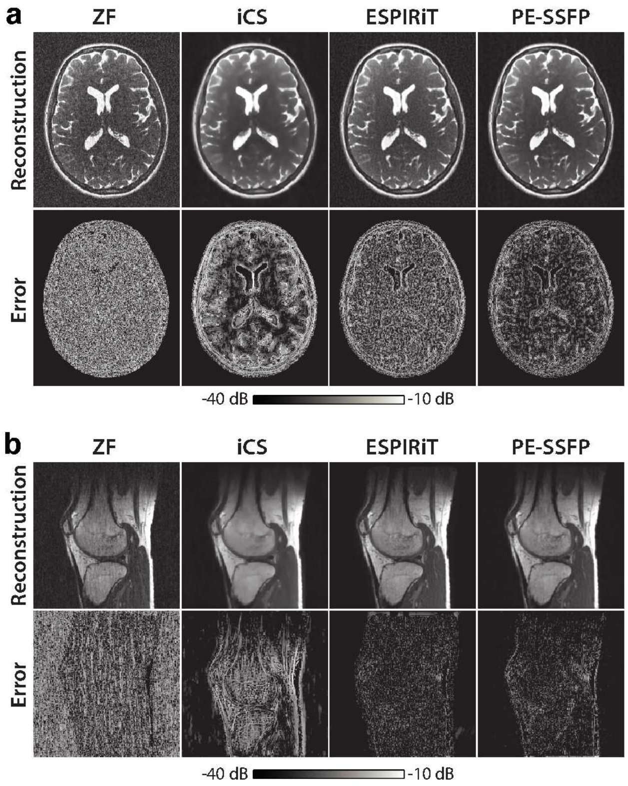

Figure 8: In vivo phase-cycled bSSFP reconstructions of the brain **(a)** and the knee **(b)** are displayed for N=8. ZF and ESPIRiT reconstructions suffer from broadly distributed reconstruction error across the images. Meanwhile, iCS reconstructions show substantial loss of high-spatial-frequency information and coherent low-frequency interference. In contrast, PE-SSFP effectively reduces errors due to aliasing and noise interference, while maintaining detailed tissue depiction.

## List of Supporting Tables

Supporting Table S1: Reconstruction Times

Supporting Table S2: Regularization Parameters

Supporting Table S3: Image Quality: Contribution of PE-SSFP projections

Supporting Table S4: Image Quality: Sampling Patterns

Supporting Table S5: Image Quality: Variations in Tissue and Sequence Parameters

Supporting Table S6: Image Quality: Acceleration Factor

## List of Supporting Figures

Supporting Figure S1: Undersampled acquisitions of the numerical brain phantom were reconstructed using PE-SSFP. The percentage difference between the reconstructed images in consecutive iterations fell to 0.001% within 15 iterations. The evolution of the PE-SSFP cost terms (calculated after the data-consistency projection) across these iterations are shown for N=2-8: **(a)** joint-sparsity cost, **(b)** TV cost, **(c)** combined cost in Eq. 6. The cost at each iteration is displayed as mean±std across 10 cross sections. The cost terms diminish smoothly across iterations.

Supporting Figure S2: The auto-calibration approach was demonstrated by examining how well the acquired data can be represented via the bSSFP profiles estimated from calibration data. A separate error map was first calculated between the fully-sampled image at each phase cycle and its projection onto the subspace spanned by the bSSFP profiles. These individual error maps were then sum-of-squares combined across phase cycles. Representative maps are shown for N=4. **(a)** Actual bSSFP profiles for each phase-cycle. **(b-d)** Individual and combined error maps for varying calibration-kernel sizes ([5, 8, 11]), calibration-area sizes ([2%, 6%, 10%] of the maximum spatial frequency), and null-space cut-offs ($\sigma_{cutoff}$=2x$10^{-1}$, 9x$10^{-2}$, 2x$10^{-2}$). The relatively small calibration area/kernel size and high $\sigma_{cutoff}$ in **b** cause prominent low- and high-spatial-frequency errors, whereas the more optimal parameters in **d** (those used in PE-SSFP) significantly dampen the low-spatial-frequency errors. In all cases, relatively higher errors occur in the vicinity of banding artifacts in individual maps. Because banding artifacts for distinct phase-cycles are in non-overlapping locations, the combined maps show a rather uniform error distribution.

**R2.1**: *New figure*

Supporting Figure S3: The success of the auto-calibration approach in estimating bSSFP profiles was analyzed for a broad range of calibration-kernel sizes, calibration-area sizes and null-space cut-offs. Representative error maps combined across phase-cycles are shown for N=8. **(a)** Error maps for different calibration-kernel sizes. **(b)** Error maps for different calibration-area sizes. **(c)** Error maps for different null-space cut-offs. PE-SSFP parameters are emphasized in bold font within each panel. The errors predominantly occur in regions of sharp signal transition near tissue boundaries. **R2.1**: *Caption revised*

# Profile-Encoding Reconstruction for Multiple-Acquisition Balanced Steady-State Free Precession (bSSFP) Imaging

Efe Ilicak[1,2], Lutfi Kerem Senel[1], Erdem Biyik[1], Tolga Çukur[1,2,3]

[1]Department of Electrical and Electronics Engineering, Bilkent University, Ankara, Turkey
[2]National Magnetic Resonance Research Center (UMRAM), Bilkent University, Ankara, Turkey
[3]Neuroscience Program, Bilkent University, Ankara, Turkey

*Running title:* Profile-Encoding Reconstruction for Multiple-Acquisition bSSFP

*Address correspondence to:*
Tolga Çukur
Department of Electrical and Electronics Engineering, Room 304
Bilkent University
Ankara, TR-06800, Turkey
TEL: +90 (312) 290-1164
E-MAIL: cukur@ee.bilkent.edu.tr

This work was supported in part by a Marie Curie Actions Career Integration Grant (PCIG13-GA-2013-618101), by a European Molecular Biology Organization Installation Grant (IG 3028), and by the Turkish Academy of Sciences through a TUBA-GEBIP 2015 fellowship awarded to T. Çukur.

Word Count: 190 (abstract), 5000 (body)
Figure and Table Count: 10

Revised submission on September 2, 2016 to *Magnetic Resonance in Medicine*.

## Abstract

**Purpose:** The scan-efficiency in multiple-acquisition bSSFP imaging can be maintained by accelerating and reconstructing each phase-cycled acquisition individually, but this strategy ignores correlated structural information among acquisitions. Here an improved acceleration framework is proposed that jointly processes undersampled data across N phase cycles.

**Methods:** Phase-cycled imaging is cast as a profile-encoding problem, modeling each image as an artifact-free image multiplied with a distinct bSSFP profile. A profile-encoding reconstruction (PE-SSFP) is employed to recover missing data by enforcing joint sparsity and total-variation penalties across phase cycles. PE-SSFP is compared with individual compressed-sensing (iCS) and parallel-imaging (ESPIRiT) reconstructions.

**Results:** In the brain and the knee, PE-SSFP yields improved image quality compared to iCS and other tested methods particularly for higher N values. On average, PE-SSFP improves peak SNR by 3.8±3.0 dB (mean±s.e. across N=2-8) and structural similarity by 1.4±1.2% over iCS, and peak SNR by 5.6±0.7 dB and structural similarity by 7.1±0.5% over ESPIRiT.

**Conclusion:** PE-SSFP attains improved image quality and preservation of high-spatial-frequency information at high acceleration factors, compared to conventional reconstructions. PE-SSFP is a promising technique for scan-efficient bSSFP imaging with improved reliability against field inhomogeneity.

**Keywords: SSFP, banding artifact, magnetization profile, compressed sensing, encoding, reconstruction**

# Introduction

Balanced steady-state free precession (bSSFP) sequences provide relatively high magnetization levels for repetition times (TR) on the order of several milliseconds (1). As such, they have found use in rapid imaging involving both dynamic (2–6) and high-spatial-resolution static acquisitions (7–11). One critical concern, however, is that the bSSFP magnetization profile yields increased sensitivity to magnetic field inhomogeneities and signal voids at particular off-resonance frequencies (1). In turn, this profile can lead to excessive banding artifacts at high field strengths, with long TRs, and in complex tissue geometries.

Several innovative methods were previously proposed to alleviate bSSFP banding artifacts. These methods include modified pulse sequences that reshape magnetization profiles (12–15), advanced shimming procedures that limit field inhomogeneity (16), physical signal models to remove frequency sensitivity (17, 18), and the commonly used multiple-acquisition methods that combine several phase-cycled images with nonoverlapping banding artifacts to improve signal homogeneity (19–24). These approaches typically compromise between artifact reduction and scan efficiency. For instance, residual banding artifacts in multiple-acquisition methods can be reduced by increasing the number of phase cycles (N). However, with higher N, the overall scan time is considerably prolonged.

To mitigate banding artifacts while maintaining scan efficiency, two recent studies proposed to accelerate phase-cycled bSSFP acquisitions (25, 26). In the first study (25), we leveraged individual compressed-sensing (CS) reconstructions to recover nonacquired bSSFP data for each phase cycle separately (27–29). In the second study (26), individual acquisitions were instead accelerated via simultaneous multi-slice imaging. While high image quality was demonstrated for low acceleration factors (around 2-4), data from separate phase-cycles were reconstructed independently in both studies. Because independent reconstructions ignore structural information that is inherently correlated across multiple acquisitions (30–32), image quality can be degraded at high acceleration factors that are critically needed with increasing N.

Here we propose an improved framework for accelerating phase-cycled bSSFP imaging that jointly reconstructs undersampled data across multiple acquisitions. Analogous to parallel imaging that takes each coil image as the product of the tissue image with a respective coil sensitivity (33), this framework models each phase-cycled bSSFP image as the product of the banding-artifact-free image with a respective bSSFP spatial profile (34, 35). Thus, inspired by recent approaches for multi-coil imaging (32), the joint reconstruction is cast as a profile-encoding problem (PE-SSFP) where nonacquired k-space samples are linearly synthesized from acquired data. To further alleviate aliasing and noise interference, PE-SSFP leverages joint-sparsity and total-variation penalties. Comprehensive simulations are presented to demonstrate the reliability of PE-SSFP against variations in sequence and tissue parameters, noise, and field inhomogeneity. Phantom and in vivo results clearly indicate that the proposed framework yields improved image quality over conventional reconstructions.

# Methods

The goal of the current study is to implement robust, artifact-free multiple-acquisition bSSFP imaging within a total scan time equivalent to a single acquisition. Starting with an overview of phase-cycled bSSFP imaging, the following sections discuss the sampling and reconstruction strategies proposed towards this goal.

## Multiple-Acquisition Phase-Cycled bSSFP Imaging

In multiple-acquisition bSSFP, several images with different phase-cycling are acquired such that banding artifacts are spatially non-overlapping across acquisitions. Assuming TE=TR/2, the fully-sampled images at each phase cycle can be expressed as (36):

$$S_n(r) = M(r)\frac{e^{i(\phi(r)+\Delta\phi_n)/2}\left(1 - A(r)e^{-i(\phi(r)+\Delta\phi_n)}\right)}{1 - B(r)\cos(\phi(r) + \Delta\phi_n)} \tag{1}$$

where $r$ denotes spatial location, $\phi(r)$ is phase accrued in a single TR due to field inhomogeneity, and $\Delta\phi_n$ is the phase-cycling value used for the $n^{th}$ acquisition where $n \in$ [1 N]. The remaining terms $M$, $A$, $B$ depend on sequence and tissue parameters. Tailored image combination techniques are then used to minimize the dependence of the bSSFP signal on $\phi(r)$ (20, 22). An artifact-free image ($S_o$) could be obtained under the condition that $\phi(r) + \Delta\phi_n = \pi$, which in turn would yield:

$$S_o(r) = iM(r)\frac{1 + A(r)}{1 + B(r)} \tag{2}$$

Thus, each phase-cycled image $S_n$ can be modeled as the multiplication of $S_o$ with a respective bSSFP profile, $C_n$ as illustrated in Fig. 1:

$$C_n(r) = \frac{S_n(r)}{S_o(r)} = \frac{e^{i(\phi+\Delta\phi_n-\pi)/2}\,(1 + B)\left(1 - Ae^{-i(\phi+\Delta\phi_n)}\right)}{(1 + A)(1 - B\cos(\phi + \Delta\phi_n))} \tag{3}$$

Combination techniques for multiple-acquisition bSSFP typically assume that data are either fully-sampled (20–22) or else adequately reconstructed (25). Estimation of bSSFP profiles has therefore not been of particular interest, apart from cases where signal-to-noise ratio (SNR) optimization or fat-water separation is aimed (23, 34). Nonetheless, the bSSFP profiles can be interpreted as a means to perform spatial encoding (35), similar to that implemented by the coil sensitivities in parallel imaging (33). With this interpretation, we cast the joint reconstruction of undersampled phase-cycled acquisitions as a profile-encoding problem:

$$y_n(k) = \mathcal{F}_n \left\{ C_n(r) \cdot S_o(r) \right\} \tag{4}$$

Here $k$ indicates k-space location, $y_n$ are the k-space data for the n$^{th}$ acquisition, and $\mathcal{F}$ is a Fourier-transform operator. For simplicity, we did not consider the effects of coil sensitivities on the joint reconstruction. Thus, assuming that bSSFP spatial profiles can be estimated based on fully-sampled central k-space data (37, 38), they can be used to solve an inverse problem that recovers the artifact-free bSSFP image $S_o(r)$ given a collection of phase-cycled data $y_n(k)$.

## Undersampling Patterns for Multiple-Acquisition bSSFP Data

Each of N separate phase-cycled acquisitions were undersampled by a factor of R=N. Sampling patterns for phase-cycled acquisitions can be selected independently. A common pattern for all acquisitions can better enforce consistency in the sampling matrix across phase-cycles, and reduce interpolation errors. On the other hand, disjoint patterns across acquisitions can expand k-space coverage, and reduce aliasing artifacts (25). To optimize sampling strategy, we compared reconstructions of data undersampled with common versus disjoint patterns. Patterns were generated using uniform-density deterministic (33, 35), variable-density random (28), and Poisson-disc sampling (32). In all cases, isotropic acceleration was performed in two dimensions, and a central k-space region spanning up to 10% of the maximum spatial frequency in each axis was fully sampled. In uniform-density sampling, the full sampling matrix was linearly ordered and then undersampled by holding every N$^{th}$ sample (e.g., 1, N+1,...). Disjoint patterns were generated by incrementing the starting index by 1 sample (35). In variable-density sampling, random patterns were generated based on a polynomial probability density function (PDF), and sampling patterns were selected among 2000 candidate patterns to minimize aliasing energy (39). Disjoint patterns were selected by minimizing both the aliasing energy for each pattern and the pair-wise correlation among patterns (25). In Poisson sampling, a polynomial PDF was used to generate a random sampling pattern that maintains locally-uniform inter-sample distances. Disjoint patterns were generated by using a distinct starting seed for the sampling algorithm (32).

## Profile-Encoding Reconstruction

In a recent study, we proposed to alleviate banding artifacts by combining separate CS reconstructions of individual phase-cycled bSSFP acquisitions (25). The individual-CS reconstruction (iCS) was implemented via a Lagrangian formulation:

$$\min_{m_n} \quad \|y_n - \mathcal{F}_{\mathcal{P}_n}\{m_n\}\|_2^2 + \lambda_1\|\psi\{m_n\}\|_1 + \lambda_2\|\nabla\{m_n\}\|_1 \tag{5}$$

This formulation comprised a data-consistency term (where $y_n$ is the acquired data, $\mathcal{F}_{\mathcal{P}_n}$ is the partial Fourier operator, and $m_n$ is the reconstructed image for the n$^{th}$ phase cycle), a sparsity term (where $\psi$ is a wavelet-transform operator), and a total-variation term (TV; where $\nabla$ is the finite difference operator). While iCS was shown to maintain good reconstruction quality for small N, loss of high-spatial-frequency information became prominent for N≥4 due to increasingly heavier undersampling factors (25).

To address this limitation, we propose a profile-encoding bSSFP (PE-SSFP) reconstruction that solves the problem in Eq. 4 by synthesizing missing k-space samples from acquired data. First, an interpolation operator estimated from calibration data is used to iteratively synthesize nonacquired data across phase-cycles. Inspired by the SPIRiT model (iterative self-consistent parallel imaging) (32), the iterative estimation procedure enforces the consistency of reconstructed data with both the acquired and the calibration data. Lastly, PE-SSFP leverages joint sparsity (30, 31, 40) and TV penalties (28) to dampen aliasing and noise interference. Here PE-SSFP was implemented as a constrained optimization problem:

$$\begin{aligned} \min_{m} \quad & \lambda_1\left\|\sqrt{\sum_n |\psi\{m_n\}|^2}\right\|_1 + \lambda_2\sum_n \|\nabla\{m_n\}\|_1 \\ \text{subj. to} \quad & \|(\mathcal{G} - I)\{m\}\|_2^2 = 0 \\ & \sum_n \|y_n - \mathcal{F}_{\mathcal{P}_n}\{m_n\}\|_2^2 = 0 \end{aligned} \tag{6}$$

where $m$ is the aggregate vector containing $m_n$ across all phase-cycles. The objective comprises a joint sparsity term and a cumulative TV term across phase cycles. The first constraint enforces consistency of reconstructed data with the calibration data (where $\mathcal{G}$ is the aggregate interpolation operator, $I$ is the identity operator). Meanwhile, the second constraint enforces cumulative data-consistency across phase cycles.

To efficiently solve the constrained optimization formulated in Eq. 6, we leveraged an alternating projection-onto-sets scheme with the aim to produce a quasi-optimal solution at the intersection of multiple sets (40). The optimization was split into four projection operators, namely calibration consistency, joint sparsity, TV, and data consistency projections. These projections were successively repeated to enforce relevant properties in the reconstructed data (see Fig. 2).

*Calibration consistency:* Prior to reconstruction, an interpolation kernel for profile encoding ($\mathcal{K}$) was obtained from aggregate calibration data $y_{calib}$ (designated as the fully-sampled part of central k-space). Kernel weights that capture linear relationships among 11×11 neighborhoods of k-space samples were estimated based on the calibration constraint $(\mathcal{K} - I).y_{calib} = 0$. A 13×13 kernel was used at N=2 to leverage the relatively higher sampling density in central k-space. The solution of this inverse problem was obtained via Tikhonov regularization (with weight $\alpha = 0.01$) to enhance noise resilience and conditioning (40). Finally, an image-space operator $\mathcal{G}$ equivalent to the trained k-space kernel $\mathcal{K}$ was computed. During reconstruction, calibration-consistency projections were implemented by applying $\mathcal{G}$ on the image reconstructed in the previous iteration, $m^{(k)} = \mathcal{G}\left\{m^{(k-1)}\right\}$.

*Joint sparsity:* Assuming insignificant motion between separate acquisitions, tissue boundaries and sparsity patterns are expected to appear in identical locations across phase-cycled images. To leverage this correlated structural information, we utilized a joint-sparsity model that has been shown to offer benefits in other MR applications (30–32, 41, 42). During PE-SSFP, the joint-sparsity term in Eq. 6 based on the Daubechies 4 wavelet can offer increased detection sensitivity for relatively small coefficients shared across phase cycles.

Wavelet-domain sparsity is conventionally enforced via shrinkage methods based on hard- $S_h(x) = \frac{x}{|x|-\lambda}.\max(0, |x| - \lambda)$ or soft-thresholding $S_s(x) = \frac{x}{|x|}.\max(0, |x| - \lambda)$, where $\lambda$ is the threshold (43).

Both functions null wavelet coefficients below $\lambda$, potentially reducing detection sensitivity for small coefficients. To alleviate this issue, here we used a modified Huber function (44) :

$$S_{huber}(x) = \begin{cases} x^2/(2\lambda) & , |x| < \lambda \\ |x| - \lambda/2 & , \text{otherwise} \end{cases} \tag{7}$$

This function behaves similarly to soft-thresholding above $\lambda$, but it applies squared-weighting on small coefficients to increase detection sensitivity. Note that iterative thresholding based on this function provides a quasi-proximal mapping for the $\ell_1$-norm, thus $\lambda$ was set to $\lambda_1$ in Eq. 6. During PE-SSFP, the following joint-sparsity projections were applied: $m^{(\dot{k})} = \psi^{-1}\left\{S_{huber}(\psi\{m^{(k)}\})\right\}$.

*TV:* Total-variation projections were employed to reduce aliasing interference and noise. The projections were implemented by minimizing the objective $J(x) = \|m_n - x\|_2^2 + \lambda_2\|\nabla x\|_1$ using a fast iterative-clipping algorithm:

$$\begin{aligned} x^{(i)} &= m_n^{(\dot{k})} - \nabla^t z^{(i-1)} \\ z^{(i)} &= S_{clip}\left(z^{(i-1)} + \nabla x^{(i)}/\alpha\right) \end{aligned} \tag{8}$$

where $\nabla^t$ is the adjoint finite-difference operator, $z^{(1)} = 0$ and the update rate parameter $\alpha = 8$ (45). The clipping function was modified to handle complex values:

$$S_{clip}(z) = \begin{cases} z & , |z| < \lambda_2/2 \\ (\lambda_2/2) \cdot exp(j\angle(z)) & , \text{otherwise} \end{cases} \tag{9}$$

where $\angle(z)$ is the phase of $z$. This algorithm converges rapidly, and the percentage change in the objective fell to 0.01% within 5 iterations during each TV projection: $m^{(\ddot{k})} = TV_{proj}\left\{m^{(\dot{k})}\right\}$.

*Data consistency:* To ensure consistency of reconstructed and acquired k-space data, reconstructed data were projected onto the constraint $\sum_n \|y_n - \mathcal{F}_{\mathcal{P}n}\{m_n\}\|_2^2 = 0$. This projection was implemented by replacing reconstructed data with the acquired data in sampled locations (40): $m^{(\ddot{k})} = \mathcal{F}^{-1}\left\{(\mathcal{F} - \mathcal{F}_{\mathcal{P}})\{m^{(\ddot{k})}\} + y\right\}$.

The successive projections listed above were repeated until the percentage difference between the reconstructed images in consecutive iterations fell to 0.001%. Convergence was achieved within 15 iterations for the datasets considered here (see Sup. Fig. S1 for typical changes in joint sparsity, TV and cumulative cost terms during PE-SSFP). The total reconstruction times are listed in Sup. Table S1. The penalty weights $\lambda_{1,2}$ were varied separately in the range $[0\ 10] \times 10^{-3}$ with a step size of $10^{-3}$ for phantom data, and in the range $[0\ 15] \times 10^{-3}$ with a step size of $0.05{\times}10^{-3}$ for in vivo data (39). To minimize potential block artifacts and resolution losses, the smallest set of $\lambda_{1,2}$ that yielded satisfactory artifact/noise suppression were selected via visual inspection (see Sup. Table S2). To obtain a final bSSFP image, reconstructions for each phase-cycle were combined with the p-norm method (p=4), which was selected for its computational simplicity and favorable performance in artifact suppression and SNR efficiency (34).

## Alternative Reconstructions

To comparatively demonstrate PE-SSFP, zero-filled Fourier (ZF), individual CS (iCS) and ESPIRiT (46) reconstructions were also implemented. All methods reconstructed individual phase-cycled images that were then p-norm combined (p=4).

*ZF:* Nonacquired k-space data were filled with zeros. Data for each phase-cycle were compensated for the sampling density across k-space. An inverse Fourier transformation was then performed to reconstruct each phase-cycled image.

*iCS:* Individual CS reconstructions of phase-cycled acquisitions were implemented as described in Eq. 5. The sparsifying transform was selected as the Daubechies 4 wavelet. The optimization was performed using an iterative conjugate-gradient algorithm (28). Iterations were repeated until the percentage difference between the reconstructed images in consecutive iterations fell to 0.01%. Convergence was achieved within 30 iterations for the datasets considered here. Further iterations were avoided because they were observed to cause undesirable blurring in the reconstructions. The regularization weights were scaled proportionately to those in PE-SSFP. Specifically, $\lambda_1$ was set to maintain the same ratio of sparsity to data-consistency terms ($\sqrt{N} \times \lambda_{1,PE-SSFP}$), $\lambda_2$ was set to maintain the same ratio of TV to data-consistency terms ($\lambda_{2,PE-SSFP}$).

*ESPIRiT:* A soft-SENSE reconstruction (33) based on multiple sets of bSSFP profiles was implemented using the $\ell_1$-ESPIRiT framework (46). Profile estimates were obtained via eigenvector decomposition of $\mathcal{G}$ in the image domain. Separate sets of profile estimates were obtained for each phase cycle ($\hat{C}_n^j$ for the $j^{th}$ set, $j \in [1\ J]$), by selecting eigenvalues above a fixed threshold of 0.9 with a null-space cut-off $\sigma^2_{\text{cutoff}}$=0.02. This yielded two sets of bSSFP profiles estimates for the datasets reported here. Individual phase-cycled images $m_n$ were then reconstructed via the following optimization:

$$\min_{m} \quad \sum_n \|y_n - \mathcal{F}_{\mathcal{P}_n}\{m_n\}\|_2^2 + \lambda_1 \left\| \sqrt{\sum_n |\psi\{m_n\}|^2} \right\|_1 \tag{10}$$

where $m_n = \sum_j \hat{C}_n^j m_n^j$. Variable splitting with a splitting parameter of 0.4 was implemented to decompose the optimization into two subproblems that minimize the profile-encoding cost (first term in the objective) and the joint-sparsity cost (second term) respectively (47). The profile-encoding subproblem was solved via a conjugate gradient algorithm with 20 iterations (40). Remaining reconstruction parameters including the number of outer iterations were kept identical to PE-SSFP.

## Simulations

Simulations were performed based on a realistic brain phantom at 0.5 mm isotropic resolution (http://www.bic.mni.mcgill.ca/brainweb). Phase-cycled bSSFP signals for each tissue were calculated based on Eq. 1, assuming the following $T_1/T_2$: 3000/1000 ms for cerebro-spinal fluid (CSF), 1200/250 ms for blood, 1000/80 ms for white matter, 1300/110 ms for gray matter, 1400/30 ms for muscle, and 370/130 ms for fat. Meanwhile, three-dimensional (3D) acquisitions were simulated using $\alpha = 45^o$ (flip angle), TR = 5.0 ms, TE = 2.5 ms, 10 axial cross-sections equispaced to cover the whole brain in the superior-inferior direction, and $\Delta\phi = 2\pi\frac{[0:1:(N-1)]}{N}$. The simulations used a realistic field-inhomogeneity distribution corresponding to an off-resonance shift of 0±62 Hz (mean±std; see Fig. 1).

To demonstrate the auto-calibration approach used in PE-SSFP, we examined how well the acquired data can be represented via the bSSFP profiles estimated from calibration data. Using the profiles extracted by the ESPIRiT method (46), each phase-cycled image was projected onto the subspace spanned by the bSSFP profiles. A difference map was then calculated between each image and its projection onto this subspace. An aggregate error map was finally formed via sum-of-squares combination of difference maps across phase cycles. Error maps were generated for varying kernel sizes (5, 7, 9, 11, 13, 15, 17), calibration area sizes (6%, 8%, 10%, 12%, 14% of the maximum spatial frequency), and null-space cut-offs ($\sigma^2_{\text{cutoff}}$=2x$10^{-1,-2,-3,-4,-5}$).

Next, simulated brain images were undersampled by a factor of N in two phase-encode dimensions using patterns generated for uniform-density, variable-density, and Poisson disc sampling. Separate acquisitions were obtained for common and disjoint sampling patterns across phase cycles. PE-SSFP and alternative reconstructions were performed.

Reconstruction quality was assessed by several different metrics measured on combined bSSFP images. For a given cross-section, a mean-squared error (MSE) was first measured between the image reconstructed from N undersampled acquisitions and a reference image Fourier reconstructed from N=8 fully-sampled acquisitions. Because N=8 is typically sufficient for artifact suppression, MSE assessed the reconstruction performance in reducing banding artifacts in addition to aliasing/noise interference. The peak signal-to-noise (PSNR) metric was then derived from this MSE measurement to summarize the overall image quality. Lastly, a mean structural similarity index (SSIM) was measured between the reconstructed image and the reference image for N=8, following histogram matching to account for large-scale intensity variations (25). SSIM assessed the degree of visual similarity in tissue structure to the reference image. To assess the reliability of PE-SSFP against field inhomogeneity, residual banding artifacts were evaluated on combined bSSFP images. CSF, white matter and gray matter signals were segregated via tissue masks. The level of residual artifact for each tissue was then characterized based on a percentage ripple metric. Ripple was taken as the ratio of the range of signal intensity to the mean intensity level. All metrics were pooled across 10 cross-sections in the phantom.

Several variants of PE-SSFP were implemented to assess the relative importance of the individual projection stages of the proposed method: PE$_{calib}$ with only calibration and data-consistency projections; PE$_{huber}$ with calibration, sparsity (based on Huber thresholding) and data-consistency projections; PE$_{soft-TV}$ with calibration, sparsity (based on soft thresholding), TV and data-consistency projections. Each additional projection included in PE-SSFP significantly improved the PSNR and SSIM values ($p<0.005$, signed-rank test; see Sup. Table S3). Furthermore, PE-SSFP outperformed that PE$_{soft-TV}$ for all N>2 ($p<0.005$). Thus, Huber thresholding was prescribed for all PE-SSFP reconstructions thereafter.

To examine the effect of tissue and sequence parameters on reconstruction performance, additional simulations were performed based on varying $T_1/T_2$ ratios, flip angles, TRs (with TE = TR/2), SNR levels, and acceleration factors (R). The following parameters were considered: (-40%, -20%, 0%, 20%, 40%) deviation in $T_1/T_2$ ratios, $\alpha = (15^o, 30^o, 45^o, 60^o, 75^o)$, TR = (5 ms, 10 ms, 15 ms), SNR levels ranging in [10 30] for CSF. To examine performance when R exceeds number of acquisitions (N), the following cases were simulated (N=2, R=4), (N=4, R=6), (N=4, R=8), and (N=6, R=8).

To evaluate noise performance, the SNR levels in the reconstructed images were compared against those in fully-sampled images. For this analysis, 30 separate noise instances with a bivariate Gaussian distribution were added to phase-cycled bSSFP images to attain acquisition SNR=20 for CSF. Each dataset was reconstructed to yield 30 separate combined bSSFP images. The SNR of each voxel was taken as the ratio of the mean to standard deviation of signal intensity across 30 images. A noise amplification map was then computed as the SNR ratio between the fully-sampled reference and reconstructed images. Significance of differences among reconstruction methods were assessed with nonparametric Wilcoxon signed-rank tests.

## In Vivo Experiments

In vivo phase-cycled bSSFP images of the brain and the knee were collected on a 3 T Siemens Magnetom scanner (maximum gradient strength of 45 mT/m and slew rate of 200 T/m/s) with a 3D Cartesian sequence. The brain imaging protocol comprised a flip angle of $30^o$, a TR/TE of 5.1/2.65 ms, a field-of-view (FOV) of 218 mm, an isotropic resolution of 0.85 mm, superior/inferior readout direction, N=8 separate acquisitions with phase-cycling values ($\Delta\phi$) spanning $[0, 2\pi)$ in equispaced intervals, and a 32-channel receive-only head coil. The knee imaging protocol comprised a flip angle of $30^o$, a TR/TE of 5.0/2.5 ms, an FOV of 192 mm, an isotropic resolution of 1 mm, left/right readout direction, N=8, and a 15-channel receive-only knee coil. Fully-sampled images were combined across coils to obtain single-channel multiple acquisition datasets. All participants gave written informed consent, and the imaging protocols were approved by the local ethics committee.

The brain and knee acquisitions were variable-density undersampled in the phase-encode dimensions to yield acceleration factors of 2-8, and profile-encoding reconstructions were performed. The following phase-cycling values were selected for reconstruction: $\Delta\phi = 2\pi\frac{[0:1:(N-1)]}{N}$ for N = 2, 4 and 8. The phase cycles for N = 6 were selected as a subset of those for N =8 (0, $\pi/2$, $3\pi/4$, $\pi$, $5\pi/4$, $7\pi/4$) to reduce overall scan time and minimize potential motion artifacts.

To examine the quality of reconstructed images, PSNR and SSIM metrics were measured across 10 equispaced cross-sections. For brain images, axial cross-sections were used that spanned across the entire volume in the superior-inferior direction. For knee images, sagittal cross-sections in the left-right direction were used. The reference image was taken as the combined Fourier reconstruction of N=8 fully-sampled acquisitions.

# Results

## Simulation Analyses

PE-SSFP was first demonstrated on bSSFP images of a numerical brain phantom. Figure 3 shows the combination bSSFP images reconstructed via ZF, iCS and PE-SSFP. As expected, heavier undersampling applied at higher N values increases aliasing interference in ZF images. Meanwhile iCS reconstructions, which process phase cycles independently, suffer from prominent losses in spatial resolution. In contrast, PE-SSFP successfully reduces aliasing interference while maintaining detailed tissue depiction even at $N = 8$.

Several complementary analyses were performed to elucidate factors contributing to reconstruction performance. To demonstrate the auto-calibration approach in PE-SSFP, errors were examined in representing acquired data in terms of the bSSFP profiles estimated from calibration data (Sup. Figs. S2 and S3). For the kernel size, calibration area and null-space cutoff prescribed in PE-SSFP, residual high-spatial-frequency errors occur near banding artifacts for each phase cycle. When combined across phase-cycles, the auto-calibration errors appear near tissue boundaries rather uniformly across the FOV. The average auto-calibration error relative to the maximum signal intensity is $3.2 \pm 0.6\%$ (mean±s.e. across N). The percentage improvement that can be attained by advancing the kernel size, calibration area or null-space cutoff to their optimal values in the tested range is merely $1.0 \pm 0.3\%$. Thus, the selected PE-SSFP parameters yield near-optimal results with relatively low error levels. To determine the effects of individual projection operators in PE-SSFP, several variant reconstructions and respective squared-error maps relative to a fully-sampled image were computed (Fig. 4). The inclusion of each projection visibly reduces error across the image. To examine noise statistics of the reconstructions, noise amplification factors were calculated across the images (Fig. 5). Although the heavier undersampling at high N increases noise in ZF, penalty terms in iCS and PE-SSFP help maintain lower noise. In PE-SSFP, relatively higher amplification is observed near tissue boundaries that are more susceptible to resolution loss due to variable-density undersampling.

To determine the effect of the sampling strategy on PE-SSFP, uniform-density, variable-density and

Poisson disc undersampling patterns were tested. Each type of pattern was applied both commonly and disjointly across phase cycles. While all sampling strategies yield similar PSNR and SSIM values at N=2 (Sup. Table S4), variable-density (VD) disjoint sampling outperforms all other methods for N>2 ($p<0.005$). VD disjoint sampling improves PSNR by 4.0±1.9 dB (mean±s.e. across N) and SSIM by 0.8±0.5% over VD common sampling, and PSNR by 3.2±1.6 dB and SSIM by 0.4±0.2% over Poisson-disc disjoint sampling. Thus VD disjoint sampling was used for all reconstructions reported here.

Finally, PE-SSFP was comparatively evaluated against ZF, iCS and ESPIRiT. Representative images for N=8 are shown in Fig. 6 along with the squared-error maps in reference to a fully-sampled image. While ZF shows broadly distributed errors across the field-of-view, iCS reduces noise and aliasing interference at the expense of losses in high-spatial-frequency information. While ESPIRiT reconstructions alleviate this loss via joint-sparsity penalties, the respective images still show distributed errors. In contrast, PE-SSFP using both joint-sparsity and TV regularization effectively dampens the reconstruction errors in phase-cycled bSSFP images.

The observations regarding PE-SSFP's superior image quality are supported by the quantitative assessments listed in Table 1. For each N, PE-SSFP yields significantly higher PSNR and SSIM values compared to all other reconstructions ($p<0.005$), with the exception of N=2 where iCS and PE-SSFP yield similar values. PE-SSFP improves PSNR by 13.1±5.0 dB and SSIM by 4.8±2.5% over iCS, and PSNR by 14.5±3.2 dB and SSIM by 3.4±0.6% over ESPIRiT. Extended simulations presented in Sup. Tables S5 and S6 indicate that these results are valid ($p<0.005$) broadly across varying flip angles ($15^o$-$75^o$), $T_1/T_2$ ratios (-40% to 40%), TRs (5-15 ms), noise levels (SNR=10-30), and when the acceleration factor exceeds N. The percentage ripple measurements listed in Table 1 indicate that PE-SSFP yields more homogeneous tissue signals compared to alternative methods for all N ($p<0.005$). Taken together, these results suggest that PE-SSFP reliably enhances image quality and artifact suppression compared to conventional reconstructions.

## In Vivo Analyses

PE-SSFP was demonstrated on bSSFP acquisitions of the brain and the knee. Similar to phantom results, the auto-calibration error was relatively low with 6.1±1.3% error (mean±s.e. across N) in the brain, and 3.7±0.7% error in the knee. Figure 7 shows the combined PE-SSFP images and the squared-error maps for N=2-8. As expected, prominent errors due to residual banding are visible for lower N values. These errors are alleviated towards high N, while maintaining high-quality tissue depiction. Representative images from ZF, iCS, ESPIRiT and PE-SSFP are displayed in Fig. 8. While iCS incurs losses at high spatial frequencies and coherent interference at low frequencies, ESPIRiT suffers from broadly distributed reconstruction errors across the images. In contrast, PE-SSFP visibly reduces reconstruction errors and preserves high-spatial-frequency information.

Quantitative assessments of in vivo reconstructions are listed in Table 2. In both the brain and the knee, PE-SSFP yields significantly higher PSNR and SSIM values compared to iCS for $N>2$ ($p<0.05$). PE-SSFP also improves PSNR and SSIM compared to all other alternative reconstructions for all N ($p<0.05$), with the exception of knee images at N=8 where PE-SSFP and ESPIRiT yield similar PSNR. In the brain, PE-SSFP improves PSNR by 3.0±2.6 dB and SSIM by 1.4±1.2% over iCS, and PSNR by 8.5±0.8 dB and SSIM by 7.1±0.5% over ESPIRiT. In the knee, PE-SSFP improves PSNR by 4.7±3.5 dB and SSIM by 1.8±0.6% over iCS, and PSNR by 2.8±1.2 dB and SSIM by 8.3±0.4% over ESPIRiT. Taken together, these results strongly suggest that the proposed method enables scan-efficient suppression of banding artifacts at high N values, while maintaining detailed tissue structure via the joint reconstruction.

# Discussion

Here we evaluted an improved acceleration framework for multiple-acquisition 3D bSSFP based on variable-density random undersampling in two phase-encode dimensions. In this framework, nonacquired data across phase-cycles are simultaneously synthesized using a profile-encoding reconstruction that enforces joint sparsity and TV penalties. A p-norm combination of individual phase-cycled images yields a final artifact-suppressed bSSFP image.

Several alternative approaches were previously proposed for reducing banding artifacts. One strategy is to increase the tolerable range of field inhomogeneity by modifying the bSSFP magnetization profile (12–15). Alternatively, advanced shimming procedures can be performed to directly limit field inhomogeneity (16). While both strategies aim to reduce banding artifacts during acquisition, they require complex pulse-sequence modifications and prolonged scan times. In contrast, our proposed framework can be implemented via standard bSSFP sequences without separate calibration procedures.

Improvements in scan efficiency of multiple-acquisition bSSFP have been considered in several previous reports. Recently, we proposed to undersample and individually reconstruct phase-cycled acquisitions using CS (25). The CS framework yielded high quality reconstructions up to an acceleration factor of N=4. Another study employed simultaneous multislice imaging to accelerate each acquisition separately, and similarly considered N≤4 (26). While these previous studies disregarded image features shared across phase-cycles, here we used a joint-sparsity model to enhance recovery of wavelet coefficients, and TV regularization to reduce aliasing and noise interference. Due to these advances, PE-SSFP maintains high-quality reconstructions up to N=8. Spatial encoding by coil arrays was not leveraged in the reconstructions reported here. However, if more effective artifact suppression is needed (e.g., while imaging at 7T or near air-tissue interfaces), a higher N value and a respectively higher acceleration factor might be maintained by also leveraging coil sensitivity information. Note, however, that each phase-cycled acquisition involves a fixed-duration overhead due to the preparatory RF pulses employed to reach steady state. This overhead will become more prominent for larger N values, reducing the overall scan efficiency.

With similar motivations to PE-SSFP, one earlier study proposed a SENSE-type reconstruction performed jointly across phase-cycled acquisitions, each accelerated via uniform-density undersampling (35). Sensitivity estimates were taken as the ratio of low resolution phase-cycled images to a maximum-intensity combination of these images. In contrast, here we used variable-density sampling, and we did not assume any combination model while calibrating the interpolation kernel. Our results clearly indicate that variable-density sampling offers improved performance compared to uniform sampling.

PE-SSFP can be potentially improved by addressing several limitations. First, if significant motion occurs in between separate acquisitions, image structure can be displaced across phase-cycles. These displacements may in turn violate the joint-sparsity model and yield suboptimal reconstructions. A motion-correction operator could be incorporated to alleviate motion-induced performance loss. Second, the auto-calibration approach in PE-SSFP relies on the assumption that bSSFP spatial profiles vary gradually. Rapid profile variations near tissue boundaries or bSSFP nulls can yield suboptimal interpolation operators, increasing reconstruction errors. This issue may be of particular concern with high field strengths, long TRs, and certain combinations of $T_1/T_2$ and flip angles. In such cases, the k-space calibration area could be expanded and interpolation kernels of variable widths across k-space could be used to improve accuracy of the interpolation operator (48, 49). Third, while a p-norm combination was observed to yield good artifact suppression in this study, it could be replaced with sophisticated techniques that leverage analytical signal models to further improve artifact suppression (17, 18). Lastly, optimization with the projection-onto-sets method does not guarantee convergence onto a fixed solution in the absence of overlap between the projection sets. While we observed good convergence behavior here, reconstruction stability can be improved by modern approaches such as the alternating direction method of multipliers (50).

In conclusion, the proposed PE-SSFP framework jointly reconstructs multiple-acquisition bSSFP data by leveraging shared sparsity patterns across phase-cycles. PE-SSFP was primarily demonstrated for brain and knee imaging in the current study. Nonetheless, the scan-efficient acquisitions and high-quality reconstructions enabled by PE-SSFP could improve other multiple-acquisition bSSFP applications such as peripheral angiography (51), coronary imaging (52), and fat/water separation (23, 53).

## Acknowledgment

The authors thank A. Emek for his contributions to the initial implementation of this work, and E.U. Saritas for helpful discussions regarding the manuscript. The authors also thank the reviewers for their insightful suggestions that significantly improved the manuscript.

# References

[1] Scheffler K, Lehnhardt S. Principles and applications of balanced SSFP techniques. Eur Radiol 2003; 13:2409–2418.

[2] Peters DC, Ennis DB, McVeigh ER. High-resolution MRI of cardiac function with projection reconstruction and steady-state free precession. Magn Reson Med 2002; 48:82–88.

[3] Bieri O, Patil S, Quick HH, Scheffler K. Morphing steady-state free precession. Magn Reson Med 2007; 58:1242–1248.

[4] Koktzoglou I, Li D, Dharmakumar R. Dephased FLAPS for improved visualization of susceptibility-shifted passive devices for real-time interventional MRI. Phys Med Biol 2007; 52:277–286.

[5] Scheffler K, Seifritz E, Bilecen D, Venkatesan R, Hennig J, Deimling M, Haacke EM. Detection of BOLD changes by means of a frequency-sensitive trueFISP technique: preliminary results. NMR Biomed 2001; 14:490–496.

[6] Miller KL, Hargreaves BA, Lee J, Ress D, de Charms RC, Pauly JM. Functional brain imaging using a blood oxygenation sensitive steady-state. Magn Reson Med 2003; 50:675–683.

[7] Hargreaves BA, Gold GE, Beaulieu CF, Vasanawala SS, Nishimura DG, Pauly JM. Comparison of new methods for magnetic resonance imaging of articular cartilage. Magn Reson Med 2003; 49:700–709.

[8] Vasanawala SS, Hargreaves BA, Pauly JM, Nishimura DG, Beaulieu CF, Gold GE. Rapid musculoskeletal MRI with phase-sensitive steady-state free precession: Comparison with routine knee MRI. AJR Am J Roentgenol 2004; 184:1450–1455.

[9] Çukur T, Nishimura DG. Multiple repetition time balanced steady-state free precession imaging. Magn Reson Med 2009; 62:193–204.

[10] Heyn C, Bowen CV, Rutt BK, Foster PJ. Detection threshold of single SPIO-labeled cells with FIESTA. Magn Reson Med 2005; 53:312–320.

[11] Çukur T, Shimakawa A, Yu H, Hargreaves BA, Hu BS, Nishimura DG, Brittain JH. Magnetization-prepared IDEAL bSSFP: A flow-independent technique for noncontrast-enhanced peripheral angiography. J Magn Reson Imaging 2011; 33:931–939.

[12] Nayak KS, Lee HL, Hargreaves BA, Hu BS. Wideband SSFP: Alternating repetition time balanced steady state free precession with increased band spacing. Magn Reson Med 2007; 58:931–938.

[13] Hargreaves BA. Partially dephased SSFP for elimination of dark bands. In: Proceedings of the 16th Annual Meeting of ISMRM, Toronto, 2008. p. 1357.

[14] Benkert T, Ehses P, Blaimer M, Jakob PM, Breuer FA. Dynamically phase-cycled radial balanced SSFP imaging for efficient banding removal. Magn Reson Med 2015; 73:182–194.

[15] Sun H, Fessler JA, Noll DC, Nielsen JF. Balanced SSFP-like steady-state imaging using small-tip fast recovery with a spectral prewinding pulse. Magn Reson Med 2016; 75:839–844.

[16] Lee J, Lustig M, Kim DH, Pauly JM. Improved shim method based on the minimization of the maximum off-resonance frequency for balanced steady-state free precession (bSSFP). Magn Reson Med 2009; 61:1500–1506.

[17] Xiang QS, Hoff MN. Banding artifact removal for bSSFP imaging with an elliptical signal model. Magn Reson Med 2014; 71:927–933.

[18] Björk M, Ingle RR, Gudmundson E, Stoica P, Nishimura DG, Barral JK. Parameter estimation approach to banding artifact reduction in balanced steady-state free precession. Magn Reson Med 2014; 72:880–892.

[19] Haacke EM, Wielopolski PA, Tkach JA, Modic MT. Steady-state free precession imaging in the presence of motion: Application for improved visualization of the cerebrospinal fluid. Radiology 1990; 175:545–552.

[20] Bangerter NK, Hargreaves BA, Vasanawala SS, Pauly JM, Gold GE, Nishimura DG. Analysis of multiple-acquisition SSFP. Magn Reson Med 2004; 51:1038–1047.

[21] Elliott AM, Bernstein MA, Ward HA, Lane J, Witte RJ. Nonlinear averaging reconstruction method for phase-cycle SSFP. Magn Reson Imaging 2007; 25:359–364.

[22] Çukur T, Bangerter NK, Nishimura DG. Enhanced spectral shaping in steady-state free precession imaging. Magn Reson Med 2007; 58:1216–1223.

[23] Quist B, Hargreaves BA, Çukur T, Morrell GR, Gold GE, Bangerter NK. Simultaneous fat suppression and band reduction with large-angle multiple-acquisition balanced steady-state free precession. Magn Reson Med 2012; 67:1004–1012.

[24] Quist B, Hargreaves BA, Daniel BL, Saranathan M. Balanced SSFP Dixon imaging with banding-artifact reduction at 3 Tesla. Magn Reson Med 2015; 74:706–715.

[25] Cukur T. Accelerated Phase-Cycled SSFP Imaging With Compressed Sensing. Medical Imaging, IEEE Transactions on 2015; 34:107–115.

[26] Wang Y, Shao X, Martin T, Moeller S, Yacoub E, Wang DJJ. Phase-cycled simultaneous multislice balanced SSFP imaging with CAIPIRINHA for efficient banding reduction; doi:10.1002/mrm.26076. Magn Reson Med 2015; 0:0–0.

[27] Block KT, Uecker M, Frahm J. Undersampled radial MRI with multiple coils: Iterative image reconstruction using a total variation constraint. Magn Reson Med 2007; 57:1086–1098.

[28] Lustig M, Donoho D, Pauly JM. Sparse MRI: The application of compressed sensing for rapid MR imaging. Magn Reson Med 2007; 58:1182–1195.

[29] Çukur T, Lustig M, Nishimura DG. Improving non-contrast-enhanced steady-state free precession angiography with compressed sensing. Magn Reson Med 2009; 61:1122–1131.

[30] Liang D, Liu B, Wang J, Ying L. Accelerating SENSE using compressed sensing. Magn Reson Med 2009; 62:1574–1584.

[31] Otazo R, Kim D, Axel L, Sodickson DK. Combination of compressed sensing and parallel imaging for highly accelerated first-pass cardiac perfusion MRI. Magn Reson Med 2010; 64:767–776.

[32] Lustig M, Pauly JM. SPIRiT: Iterative self-consistent parallel imaging reconstruction from arbitrary k-space. Magn Reson Med 2010; 64:457–471.

[33] Pruessmann KP, Weiger M, Scheidegger MB, Boesiger P. SENSE: Sensitivity encoding for fast MRI. Magn Reson Med 1999; 42:952–962.

[34] Çukur T, Lustig M, Nishimura DG. Multiple-profile homogenous image combination: Application to phase-cycled SSFP and multi-coil imaging. Magn Reson Med 2008; 60:732–738.

[35] Lustig M, Santos JM, Pauly JM. A super-FOV method for rapid SSFP banding artifact reduction. In: Proceedings of the 13th Annual Meeting of ISMRM, Miami Beach, 2005. p. 504.

[36] Lauzon ML, Frayne R. Analytical characterization of RF phase-cycled balanced steady-state free precession. Concepts Magn. Reson. 2009; 34A:133–143.

[37] Ying L, Sheng J. Joint image reconstruction and sensitivity estimation in SENSE (JSENSE). Magn Reson Med 2007; 57:1196–1202.

[38] Uecker M, Hohage T, Block KT, Frahm J. Image reconstruction by regularized nonlinear inversion–joint estimation of coil sensitivities and image content. Magn Reson Med 2008; 60:674–682.

[39] Çukur T, Lustig M, Saritas EU, Nishimura DG. Signal Compensation and Compressed Sensing for Magnetization-Prepared MR Angiography. IEEE Trans Med Imaging 2011; 34:107–115.

[40] Murphy M, Alley M, Demmel J, Keutzer K, Vasanawala S, Lustig M. Fast $\ell_1$-SPIRiT compressed sensing parallel imaging MRI: scalable parallel implementation and clinically feasible runtime. IEEE Trans Med Imaging 2012; 31:1250–1262.

[41] Akçakaya M, Hu P, Chuang ML, Hauser TH, Ngo LH, Manning WJ, Tarokh V, Nezafat R. Accelerated noncontrast-enhanced pulmonary vein MRA with distributed compressed sensing. J Magn Reson Imaging 2011; 33:1248–1255.

[42] Doneva M, Börnert P, Eggers H, Stehning C, Sénégas J, Mertins A. Compressed sensing reconstruction for magnetic resonance parameter mapping. Magn Reson Med 2010; 64:1114–1120.

[43] Donoho DL, Johnstone JM. Ideal spatial adaptation by wavelet shrinkage. Biometrika 1994; 81:425–455.

[44] Yu DF, Fessler JA. Edge-preserving tomographic reconstruction with nonlocal regularization. IEEE Trans Med Imaging 2002; 21:159–173.

[45] Chambolle A. Total Variation Minimization and a Class of Binary MRF Models. *in* “Lecture Notes in Computer Science” (Rangarajan A, Vemuri B, Yuille A, Eds.), pp. 136–152–152. Springer Berlin Heidelberg, Berlin, Heidelberg, 2005.

[46] Uecker M, Lai P, Murphy MJ, Virtue P, Elad M, Pauly JM, Vasanawala SS, Lustig M. ESPIRiT–an eigenvalue approach to autocalibrating parallel MRI: where SENSE meets GRAPPA. Magn Reson Med 2014; 71:990–1001.

[47] Huang F, Chen Y, Yin W, Lin W, Ye X, Guo W, Reykowski A. A rapid and robust numerical algorithm for sensitivity encoding with sparsity constraints: self-feeding sparse SENSE. Magn Reson Med 2010; 64:1078–1088.

[48] Cukur T, Santos JM, Nishimura DG, Pauly JM. Varying kernel-extent gridding reconstruction for undersampled variable-density spirals. Magn Reson Med 2008; 59:196–201.

[49] Çukur T, Santos JM, Pauly JM, Nishimura DG. Variable-density parallel imaging with partially localized coil sensitivities. IEEE Trans Med Imaging 2010; 29:1173–1181.

[50] Boyd S, Parikh N, Chu E, Peleato B, Eckstein J. Distributed Optimization and Statistical Learning via the Alternating Direction Method of Multipliers. Found. Trends Mach. Learn. 2011; 3:1–122.

[51] Çukur T, Lee JH, Bangerter NK, Hargreaves BA, Nishimura DG. Non-contrast-enhanced flow-independent peripheral MR angiography with balanced SSFP. Magn Reson Med 2009; 61:1533–1539.

[52] Nayak KS, Hargreaves BA, Hu BS, Nishimura DG, Pauly JM, Meyer CH. Spiral balanced SSFP cardiac imaging. Magn Reson Med 2005; 53:1468–1473.

[53] Çukur T, Nishimura DG. Fat-water separation with alternating repetition time balanced SSFP. Magn Reson Med 2008; 60:479–484.

# List of Tables

Table 1: Image Assessments for the Brain Phantom

**Peak SNR and Structural Similarity**

| | | **N = 2** | **N = 4** | **N = 6** | **N = 8** |
|---|---|---|---|---|---|
| **ZF** | PSNR | 51.8±0.1 | 50.0±0.2 | 47.2±0.1 | 45.9±0.1 |
| | SSIM | 72.8±0.6 | 65.4±0.8 | 62.4±0.8 | 61.2±0.8 |
| **iCS** | PSNR | 57.5±0.5 | 61.3±0.3 | 52.3±0.4 | 49.0±0.3 |
| | SSIM | 97.9±0.1 | 97.0±0.0 | 91.4±0.3 | 88.2±0.3 |
| **ESPIRiT** | PSNR | 48.0±0.1 | 56.3±0.1 | 56.1±0.3 | 54.1±0.3 |
| | SSIM | 93.5±0.1 | 95.8±0.1 | 95.6±0.1 | 95.1±0.1 |
| **PE-SSFP** | PSNR | 57.9±0.4 | 78.2±0.3 | 71.5±0.4 | 64.9±0.3 |
| | SSIM | 98.4±0.1 | 98.8±0.0 | 98.4±0.0 | 98.0±0.0 |

**Percentage Ripple**

| | | **N=2** | **N=4** | **N=6** | **N=8** |
|---|---|---|---|---|---|
| **ZF** | CSF | 38.8±2.1 | 29.7±1.6 | 31.9±2.1 | 32.5±2.1 |
| | White | 72.9±4.0 | 94.7±6.4 | 94.0±5.3 | 97.2±6.5 |
| | Gray | 53.8±2.1 | 73.2±5.1 | 76.3±3.2 | 77.8±5.5 |
| **iCS** | CSF | 23.2±0.8 | 8.9±1.1 | 17.9±1.4 | 23.9±2.6 |
| | White | 8.5±1.1 | 21.4±3.0 | 40.9±5.9 | 48.8±4.3 |
| | Gray | 9.7±1.1 | 17.7±1.4 | 30.8±4.6 | 36.7±6.2 |
| **ESPIRiT** | CSF | 43.9±1.1 | 17.5±2.1 | 18.8±1.5 | 19.7±1.4 |
| | White | 43.7±5.8 | 41.3±7.9 | 47.2±6.3 | 51.4±8.7 |
| | Gray | 39.0±3.8 | 28.7±2.7 | 34.5±3.8 | 36.1±5.0 |
| **PE-SSFP** | CSF | 22.5±0.2 | 2.1±0.2 | 3.4±0.5 | 3.1±0.5 |
| | White | 5.4±0.4 | 5.9±0.5 | 6.3±0.7 | 6.6±0.7 |
| | Gray | 8.3±0.3 | 6.9±0.4 | 6.8±0.4 | 7.4±1.1 |

Image assessment metrics measured in reconstructed bSSFP images of the numerical brain phantom. Metrics are reported separately for each reconstruction method as mean±std across 10 cross-sections. The top panel lists the peak SNR (PSNR) and structural similarity (SSIM) measurements obtained for $\alpha = 45^o$, TR = 5 ms, fixed $T_1/T_2$ values, and a realistic off-resonance frequency map (0±62 Hz). The bottom panel lists the percentage ripple measurements for CSF, white matter and gray matter separately.

Table 2: Image Assessments for In Vivo Datasets

**Brain Images**

| | | **N=2** | **N=4** | **N=6** | **N=8** |
|---|---|---|---|---|---|
| **ZF** | PSNR | 48.6±0.2 | 44.1±0.4 | 41.4±0.4 | 40.3±0.4 |
| | SSIM | 73.5±0.6 | 56.4±0.8 | 50.6±0.7 | 48.9±0.8 |
| **iCS** | PSNR | 58.4±1.0 | 60.7±0.4 | 56.8±0.9 | 53.2±0.9 |
| | SSIM | 93.0±1.0 | 93.2±0.8 | 91.2±0.8 | 88.9±0.9 |
| **ESPIRiT** | PSNR | 49.5±0.5 | 53.4±0.4 | 51.8±0.6 | 52.5±0.5 |
| | SSIM | 84.2±0.7 | 87.6±0.8 | 84.7±0.5 | 86.7±0.7 |
| **PE-SSFP** | PSNR | 56.0±0.7 | 62.5±0.5 | 61.0±0.8 | 61.5±0.7 |
| | SSIM | 92.0±0.5 | 94.0±0.4 | 92.7±0.4 | 93.0±0.3 |

**Knee Images**

| | | **N = 2** | **N = 4** | **N = 6** | **N = 8** |
|---|---|---|---|---|---|
| **ZF** | PSNR | 59.6±0.3 | 57.8±0.5 | 55.7±0.3 | 54.4±0.4 |
| | SSIM | 86.2±0.6 | 77.2±0.9 | 72.8±1.1 | 69.2±1.1 |
| **iCS** | PSNR | 65.2±0.7 | 72.8±0.4 | 65.3±0.9 | 63.0±1.2 |
| | SSIM | 94.7±0.5 | 95.5±0.4 | 92.0±0.4 | 90.5±0.2 |
| **ESPIRiT** | PSNR | 60.5±0.4 | 68.3±0.4 | 70.7±0.6 | 74.6±0.6 |
| | SSIM | 84.5±1.2 | 87.2±2.4 | 87.2±2.4 | 87.8±2.3 |
| **PE-SSFP** | PSNR | 63.9±0.5 | 73.3±0.4 | 73.4±0.7 | 74.5±0.6 |
| | SSIM | 93.5±0.4 | 95.8±0.2 | 95.2±0.3 | 95.4±0.3 |

Image assessment metrics measured in reconstructed bSSFP images of in vivo brain and knee data. Metrics are reported separately for each reconstruction method as mean±std across 10 cross-sections. The top panel lists PSNR and SSIM measurements for brain images, and the bottom panel lists the measurements for knee images.

# List of Figures

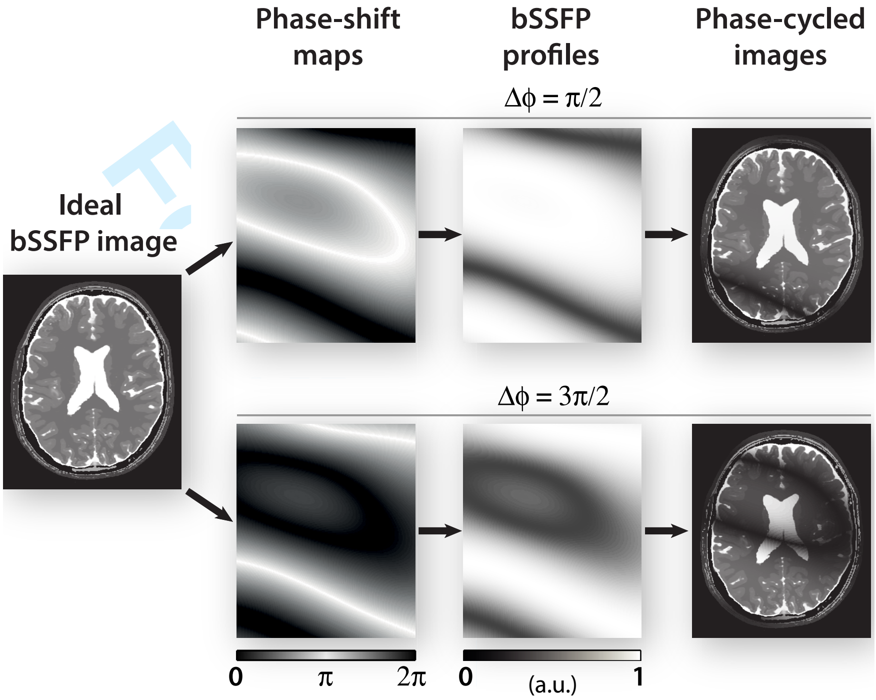

Figure 1: In the profile-encoding framework, each phase-cycled bSSFP image ($S_n$) is modeled as the multiplication of an ideal image free of banding artifacts ($S_o$) with a respective bSSFP sensitivity profile ($C_n$). The value of the bSSFP profile at each location is a function of total phase accrual over a single TR due to main field inhomogeneity and RF phase-cycling increment ($\Delta\phi$). Locations of near-zero phase shift (modulo $2\pi$) lead to significantly diminished sensitivity and thereby banding artifacts in bSSFP images.

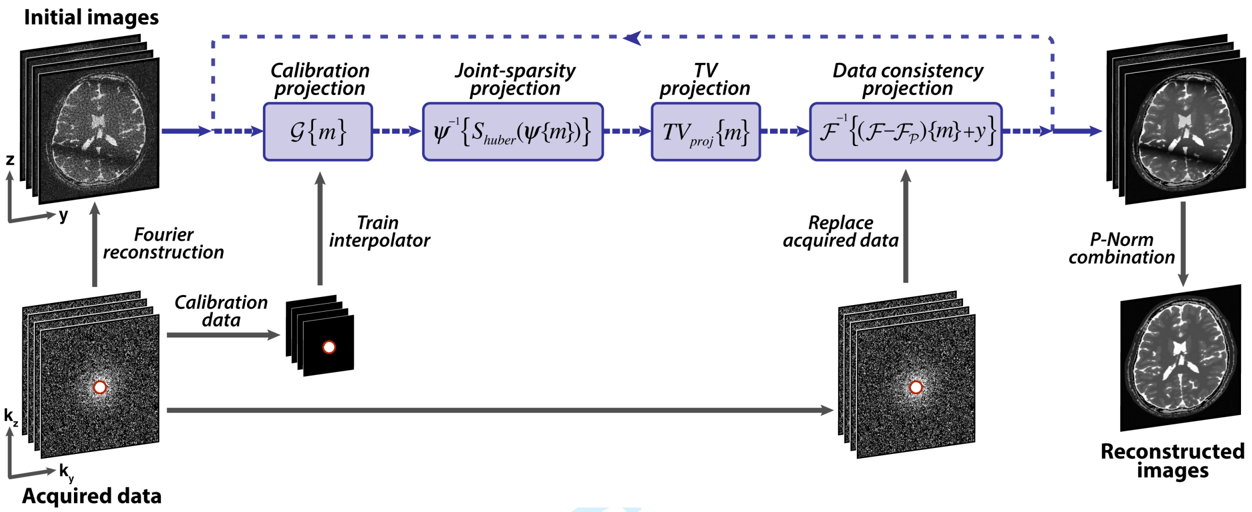

Figure 2: Flowchart of the profile-encoding bSSFP (PE-SSFP) reconstruction that recovers missing data in undersampled phase-cycled acquisitions. PE-SSFP employs an alternating projection-onto-sets scheme with four projection operators: calibration, joint-sparsity, TV, and data-consistency projections. In the calibration projection, an interpolation kernel estimated from calibration data is used to synthesize missing samples linearly from acquired data across phase-cycles. In the joint-sparsity projection, wavelet coefficients of phase-cycled bSSFP images are thresholded with a Huber function. In the TV projection, bSSFP images are denoised with a fast iterative-clipping algorithm. In the data-consistency projection, reconstructed data in sampled locations are replaced with their acquired values. These projections are successively repeated, and the individual phase-cycled images are finally combined with the p-norm method.

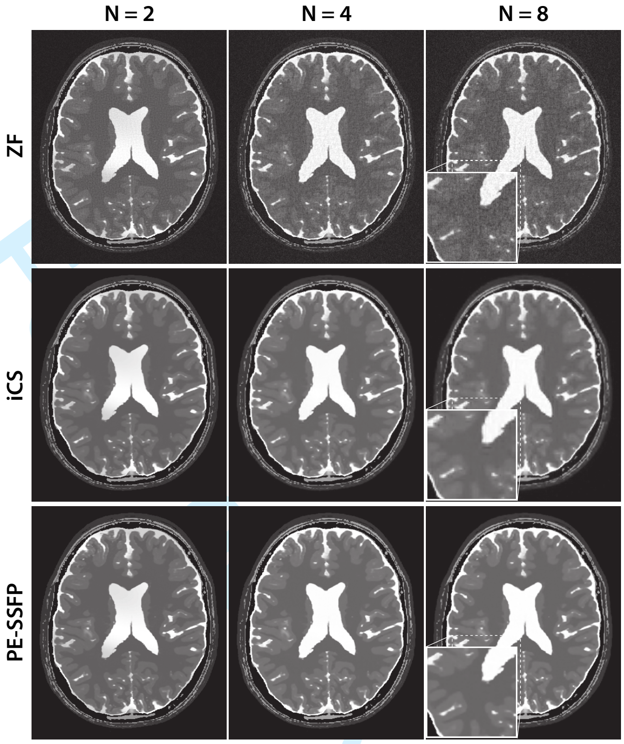

Figure 3: Phase-cycled bSSFP images of a numerical phantom were simulated for N=2-8, $\alpha = 45^o$, TR/TE=5.0/2.5 ms, a field map of 0±62 Hz (mean±std). Phantom images were undersampled by a factor of N via variable-density random sampling, disjointly across phase cycles. Zero-filled Fourier (ZF, top row), individual compressed sensing (iCS, middle row), and PE-SSFP (bottom row) reconstructions are shown. White boxes display a zoomed-in portion of the images. ZF reconstructions suffer from elevated aliasing/noise interference at high N due to the heavier undersampling factors used. While iCS reconstructions employ regularization terms that limit this interference, the heavy undersampling factors at high N cause visible loss of spatial resolution. In contrast, PE-SSFP successfully alleviates noise and aliasing interference while maintaining detailed depiction of tissue boundaries.

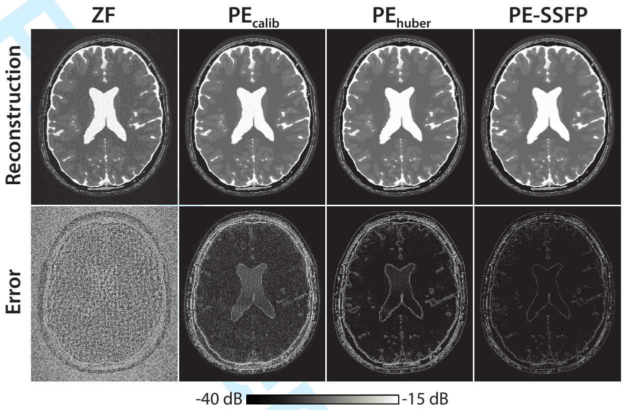

Figure 4: Representative bSSFP images of the numerical phantom for N=4 were reconstructed using ZF and PE-SSFP. Images from three variants of PE-SSFP are shown (top row). PE$_{calib}$ only uses calibration and data-consistency projections, PE$_{huber}$ uses calibration, joint-sparsity and data-consistency projections, and PE-SSFP additionally uses TV projections. Reconstructions were compared against a combination of fully-sampled images (for N=8). Squared-error maps are shown in logarithmic scale (bottom row; see colorbar). Each additional projection in PE-SSFP yields visibly reduced reconstruction error in bSSFP images.

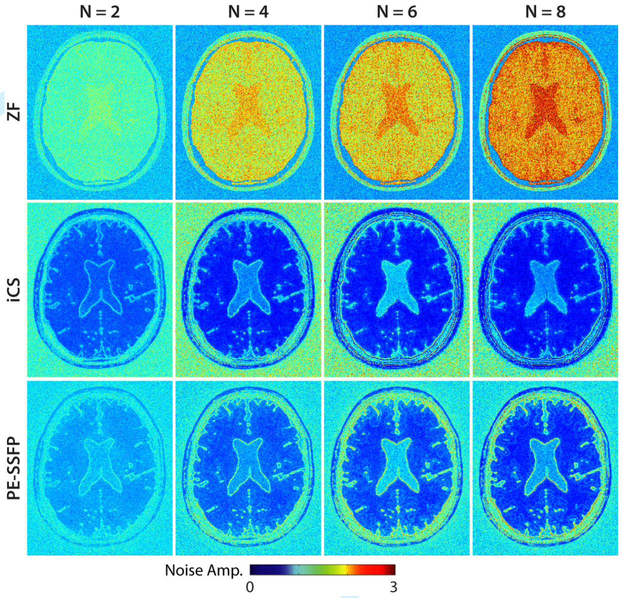

Figure 5: The noise-amplification maps for ZF, iCS and PE-SSFP methods are displayed for N=2-8. Although the heavier undersampling at high N increases noise amplification in ZF reconstructions, reconstructions with penalty terms iCS and PE-SSFP maintain relatively low noise amplification even at high N. The lower noise amplification with iCS likely reflects a bias from excessive loss of high-spatial-frequency information. In PE-SSFP, relatively higher amplification is observed near tissue boundaries that are more susceptible to resolution loss due to variable-density undersampling.

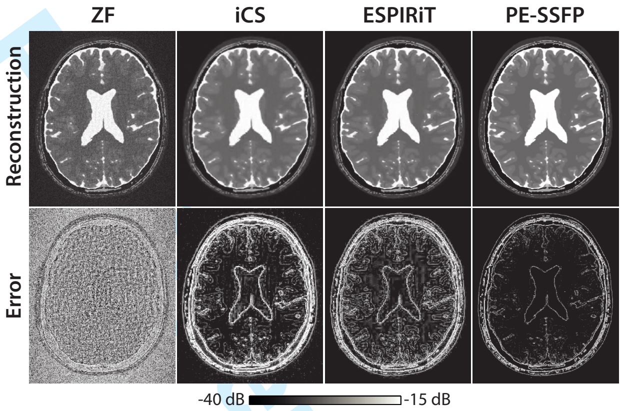

Figure 6: Phase-cycled bSSFP reconstructions of the numerical phantom (top row), and the squared-error maps with respect to the fully-sampled combination image (bottom row) are displayed for N=8. ZF has broadly distributed errors across the field-of-view due to aliasing and noise interference. iCS reconstructions reduce this interference via TV regularization at the expense of elevated errors near tissue boundaries, due to significant loss of high-spatial-frequency information. While ESPIRiT reconstructions alleviate this loss via joint-sparsity penalties, the respective images still show broadly distributed errors. In contrast, PE-SSFP using both joint-sparsity and TV regularization further dampens the reconstruction errors in phase-cycled bSSFP images.

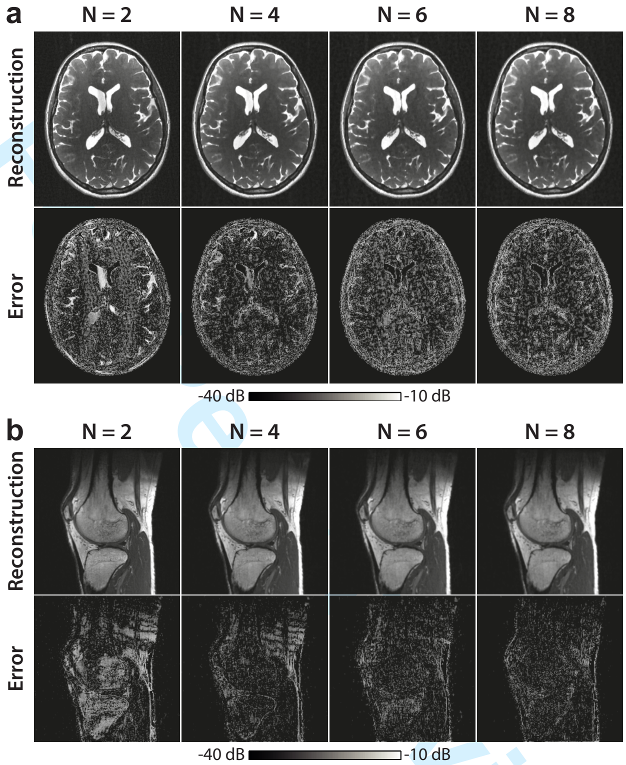

Figure 7: In vivo bSSFP acquisitions of the brain **(a)** and the knee **(b)** were reconstructed using PE-SSFP. Squared-error maps are shown in logarithmic scale (see colorbar). The error maps clearly suggest that banding artifact suppression improves for higher N, while PE-SSFP maintains detailed depiction of high-spatial-frequency information.

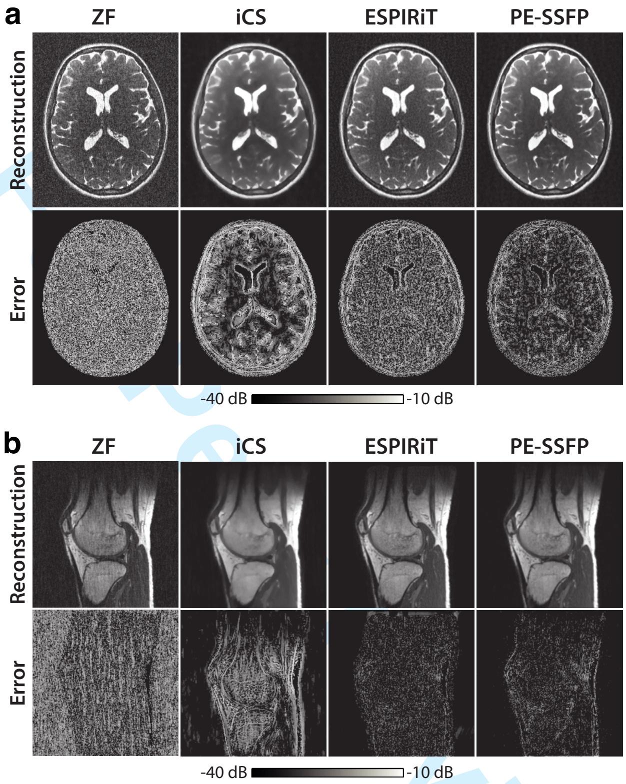

Figure 8: In vivo phase-cycled bSSFP reconstructions of the brain **(a)** and the knee **(b)** are displayed for N=8. ZF and ESPIRiT reconstructions suffer from broadly distributed reconstruction error across the images. Meanwhile, iCS reconstructions show substantial loss of high-spatial-frequency information and coherent low-frequency interference. In contrast, PE-SSFP effectively reduces errors due to aliasing and noise interference, while maintaining detailed tissue depiction.

## List of Supporting Tables

Supporting Table S1: Reconstruction Times

Supporting Table S2: Regularization Parameters

Supporting Table S3: Image Quality: Contribution of PE-SSFP projections

Supporting Table S4: Image Quality: Sampling Patterns

Supporting Table S5: Image Quality: Variations in Tissue and Sequence Parameters

Supporting Table S6: Image Quality: Acceleration Factor

## List of Supporting Figures

Supporting Figure S1: Undersampled acquisitions of the numerical brain phantom were reconstructed using PE-SSFP. The percentage difference between the reconstructed images in consecutive iterations fell to 0.001% within 15 iterations. The evolution of the PE-SSFP cost terms (calculated after the data-consistency projection) across these iterations are shown for N=2-8: **(a)** joint-sparsity cost, **(b)** TV cost, **(c)** combined cost in Eq. 6. The cost at each iteration is displayed as mean±std across 10 cross sections. The cost terms diminish smoothly across iterations.

Supporting Figure S2: The auto-calibration approach was demonstrated by examining how well the acquired data can be represented via the bSSFP profiles estimated from calibration data. A separate error map was first calculated between the fully-sampled image at each phase cycle and its projection onto the subspace spanned by the bSSFP profiles. These individual error maps were then sum-of-squares combined across phase cycles. Representative maps are shown for N=4. **(a)** Actual bSSFP profiles for each phase-cycle. **(b-d)** Individual and combined error maps for varying calibration-kernel sizes ([5, 8, 11]), calibration-area sizes ([2%, 6%, 10%] of the maximum spatial frequency), and null-space cut-offs ($\sigma_{cutoff}$=2x10$^{-1}$, 9x10$^{-2}$, 2x10$^{-2}$). The relatively small calibration area/kernel size and high $\sigma_{cutoff}$ in **b** cause prominent low- and high-spatial-frequency errors, whereas the more optimal parameters in **d** (those used in PE-SSFP) significantly dampen the low-spatial-frequency errors. In all cases, relatively higher errors occur in the vicinity of banding artifacts in individual maps. Because banding artifacts for distinct phase-cycles are in non-overlapping locations, the combined maps show a rather uniform error distribution.

Supporting Figure S3: The success of the auto-calibration approach in estimating bSSFP profiles was analyzed for a broad range of calibration-kernel sizes, calibration-area sizes and null-space cut-offs. Representative error maps combined across phase-cycles are shown for N=8. **(a)** Error maps for different calibration-kernel sizes. **(b)** Error maps for different calibration-area sizes. **(c)** Error maps for different null-space cut-offs. PE-SSFP parameters are emphasized in bold font within each panel. The errors predominantly occur in regions of sharp signal transition near tissue boundaries.

# Supporting Info For:

# Profile-Encoding Reconstruction for Multiple-Acquisition Balanced Steady-State Free Precession (bSSFP) Imaging

Efe Ilicak[1,2], Lutfi Kerem Senel[1], Erdem Biyik[1], Tolga Çukur[1,2,3]

[1]Department of Electrical and Electronics Engineering, Bilkent University, Ankara, Turkey

[2]National Magnetic Resonance Research Center (UMRAM), Bilkent University, Ankara, Turkey

[3]Neuroscience Program, Bilkent University, Ankara, Turkey

*Running title:* Profile-Encoding Reconstruction for Multiple-Acquisition bSSFP

*Address correspondence to:*
Tolga Çukur
Department of Electrical and Electronics Engineering, Room 304
Bilkent University
Ankara, TR-06800, Turkey
TEL: +90 (312) 290-1164
E-MAIL: cukur@ee.bilkent.edu.tr

This work was supported in part by a Marie Curie Actions Career Integration Grant (PCIG13-GA-2013-618101), by a European Molecular Biology Organization Installation Grant (IG 3028), and by a TUBA GEBIP fellowship awarded to T. Çukur.

Table Count: 6

Figure Count: 3

# List of Supporting Tables

| | **N = 2** | **N = 4** | **N = 6** | **N = 8** |
|---|---|---|---|---|
| **Brain (phantom)** | 19.6 s | 28.4 s | 37.8 s | 60.0 s |
| **Brain (in vivo)** | 6.6 s | 9.6 s | 13.0 s | 16.2 s |
| **Knee (in vivo)** | 6.1 s | 8.6 s | 11.8 s | 16.3 s |

PE-SSFP reconstruction times for a single cross-section are listed for phantom and in vivo data. Reconstructions were implemented in MATLAB (Mathworks, MA), on a workstation equipped with a 3.2 GHz Intel E5 processor (Intel Corporation, CA).

Supporting Table S1: Reconstruction Times

| | **N = 2** | **N = 4** | **N = 6** | **N = 8** |
|---|---|---|---|---|
| **Brain (phantom)** | 8.0, 2.0 | 8.0, 2.0 | 8.0, 2.0 | 8.0, 2.0 |
| **Brain (in vivo)** | 1.5, 15 | 1.5, 15 | 0.75, 7.5 | 0.75, 7.5 |
| **Knee (in vivo)** | 0.15, 1.5 | 0.15, 1.5 | 0.075, 0.75 | 0.075, 0.75 |

Regularization parameters $\lambda_{1,2}(\times 10^{-3})$ prescribed for PE-SSFP reconstructions are listed for each dataset and each N.

Supporting Table S2: Regularization Parameters

| | | **N = 2** | **N = 4** | **N = 6** | **N = 8** |
|---|---|---|---|---|---|
| **ZF** | PSNR | 51.8±0.1 | 50.0±0.2 | 47.2±0.1 | 45.9±0.1 |
| | SSIM | 72.8±0.6 | 65.4±0.8 | 62.4±0.8 | 61.2±0.8 |
| **PE**$_{calib}$ | PSNR | 57.3±0.2 | 63.4±0.2 | 59.7±0.2 | 56.8±0.2 |
| | SSIM | 96.1±0.1 | 94.4±0.1 | 92.4±0.1 | 92.1±0.1 |
| **PE**$_{huber}$ | PSNR | 57.7±0.3 | 69.8±0.3 | 64.6±0.4 | 59.6±0.3 |
| | SSIM | 97.9±0.1 | 98.1±0.0 | 97.3±0.0 | 96.6±0.0 |
| **PE**$_{soft-TV}$ | PSNR | 57.8±0.4 | 73.1±0.3 | 67.7±0.3 | 62.5±0.3 |
| | SSIM | 98.0±0.1 | 98.2±0.0 | 97.8±0.0 | 97.4±0.0 |
| **PE-SSFP** | PSNR | 57.9±0.4 | 78.2±0.3 | 71.5±0.4 | 64.9±0.3 |
| | SSIM | 98.4±0.1 | 98.8±0.0 | 98.4±0.0 | 98.0±0.0 |

Undersampled phantom images were reconstructed with several variants of PE-SSFP. The variants included PE$_{calib}$ (calibration and data-consistency projections), PE$_{huber}$ (calibration, sparsity -based on Huber thresholding- and data-consistency projections), PE$_{soft-TV}$ (calibration, sparsity -based on soft thresholding- TV and data-consistency projections). Peak SNR (PSNR) and structural similarity (SSIM) measurements are reported as mean±std across 10 cross sections.

Supporting Table S3: Image Quality: Contribution of PE-SSFP projections

**Peak SNR**

| | | **N=2** | **N=4** | **N=6** | **N=8** |
|---|---|---|---|---|---|
| **Uniform** | Common | 57.9±0.3 | 58.9±0.5 | 48.7±0.5 | 44.8±0.4 |
| | Disjoint | 57.9±0.3 | 66.6±0.4 | 58.1±0.7 | 52.3±0.3 |
| **Poisson** | Common | 57.9±0.3 | 74.1±0.3 | 62.5±0.3 | 57.1±0.3 |
| | Disjoint | 57.9±0.3 | 76.2±0.3 | 65.5±0.3 | 60.2±0.2 |
| **VD** | Common | 57.9±0.4 | 75.6±0.4 | 64.7±0.4 | 58.2±0.4 |
| | Disjoint | 57.9±0.4 | 78.2±0.3 | 71.5±0.4 | 64.9±0.3 |

**Structural Similarity**

| | | **N = 2** | **N = 4** | **N = 6** | **N = 8** |
|---|---|---|---|---|---|
| **Uniform** | Common | 99.2±0.1 | 95.7±0.4 | 86.5±0.5 | 82.0±0.5 |
| | Disjoint | 99.2±0.1 | 98.3±0.2 | 95.5±0.3 | 91.7±0.2 |
| **Poisson** | Common | 99.2±0.1 | 99.2±0.1 | 97.9±0.1 | 96.5±0.1 |
| | Disjoint | 99.2±0.2 | 99.3±0.1 | 98.5±0.1 | 97.6±0.2 |
| **VD** | Common | 99.3±0.1 | 99.2±0.1 | 98.1±0.1 | 96.3±0.2 |
| | Disjoint | 99.3±0.1 | 99.4±0.1 | 99.0±0.2 | 98.4±0.1 |

Phantom acquisitions were undersampled by a factor of N using either common or disjoint patterns across N phase cycles. Separate patterns were designed based on uniform-density (Uniform) sampling, Poisson-disc (Poisson) sampling, and variable-density (VD) sampling patterns. PSNR and SSIM measurements for PE-SSFP reconstructions are reported as mean±std across 10 cross sections.

Supporting Table S4: Image Quality: Sampling Patterns

**$\alpha$ = (15$^o$, 30$^o$, 45$^o$, 60$^o$, 75$^o$)**

| | | **N = 2** | **N = 4** | **N = 6** | **N = 8** |
|---|---|---|---|---|---|
| **ZF** | PSNR | 52.5±4.8 | 49.2±2.4 | 47.2±1.3 | 46.4±0.8 |
| | SSIM | 89.3±1.8 | 77.6±4.4 | 73.0±5.1 | 70.4±5.1 |
| **iCS** | PSNR | 59.7±9.6 | 58.3±4.7 | 52.1±1.9 | 49.7±0.5 |
| | SSIM | 97.7±2.6 | 97.1±1.6 | 93.7±0.3 | 91.4±0.8 |
| **ESPIRiT** | PSNR | 49.3±3.1 | 54.6±4.1 | 55.2±2.5 | 54.0±1.2 |
| | SSIM | 93.5±2.9 | 95.1±3.0 | 95.3±1.1 | 95.0±0.5 |
| **PE-SSFP** | PSNR | 61.4±11.6 | 70.6±11.4 | 69.0±7.4 | 65.0±1.7 |
| | SSIM | 98.1±2.5 | 98.9±1.5 | 98.8±0.9 | 98.4±0.2 |

**TR = (5 ms, 10 ms, 15 ms)**

| | | **N=2** | **N=4** | **N=6** | **N=8** |
|---|---|---|---|---|---|
| **ZF** | PSNR | 50.5±1.1 | 49.2±0.9 | 46.6±0.7 | 45.3±0.8 |
| | SSIM | 88.7±2.2 | 73.7±2.4 | 68.3±2.3 | 65.7±2.0 |
| **iCS** | PSNR | 55.7±1.4 | 61.7±0.2 | 52.7±0.1 | 49.3±0.1 |
| | SSIM | 99.2±0.2 | 97.8±0.1 | 93.7±0.0 | 91.1±0.1 |
| **ESPIRiT** | PSNR | 46.0±1.8 | 55.8±0.5 | 55.7±0.7 | 53.8±0.6 |
| | SSIM | 93.5±1.2 | 96.2±0.4 | 95.5±0.5 | 94.7±0.5 |
| **PE-SSFP** | PSNR | 56.0±1.6 | 76.3±2.2 | 69.7±2.2 | 63.8±1.4 |
| | SSIM | 99.3±0.2 | 99.3±0.2 | 98.9±0.3 | 98.0±0.2 |

**$T_1/T_2$ deviation (-40%, -20%, 0%, 20%, 40%)**

| | | **N = 2** | **N = 4** | **N = 6** | **N = 8** |
|---|---|---|---|---|---|
| **ZF** | PSNR | 51.9±1.3 | 50.0±0.4 | 47.3±0.3 | 46.0±0.3 |
| | SSIM | 90.9±0.8 | 76.7±1.4 | 71.0±1.2 | 68.0±0.7 |
| **iCS** | PSNR | 57.4±2.0 | 61.1±0.7 | 52.6±0.3 | 49.4±0.2 |
| | SSIM | 99.1±0.3 | 97.8±0.1 | 93.8±0.2 | 91.2±0.3 |
| **ESPIRiT** | PSNR | 48.2±0.4 | 55.9±0.7 | 56.6±1.0 | 54.6±0.9 |
| | SSIM | 94.7±0.4 | 96.6±0.6 | 96.1±0.7 | 95.3±0.7 |
| **PE-SSFP** | PSNR | 58.1±2.0 | 77.0±2.2 | 71.7±0.2 | 65.1±0.2 |
| | SSIM | 99.4±0.3 | 99.5±0.1 | 99.1±0.2 | 98.4±0.2 |

**SNR = (10, 15, 20, 25, 30)**

| | | **N=2** | **N=4** | **N=6** | **N=8** |
|---|---|---|---|---|---|
| **ZF** | PSNR | 48.9±3.4 | 46.8±3.5 | 45.6±2.7 | 44.4±2.6 |
| | SSIM | 72.8±10.2 | 66.0±9.0 | 63.8±7.9 | 62.8±6.7 |
| **iCS** | PSNR | 55.7±3.2 | 56.3±3.4 | 51.0±1.8 | 48.6±1.1 |
| | SSIM | 85.1±9.6 | 85.9±8.2 | 83.3±7.3 | 81.8±5.4 |
| **ESPIRiT** | PSNR | 49.2±1.1 | 55.2±2.9 | 54.6±2.8 | 53.4±2.0 |
| | SSIM | 85.6±8.3 | 86.7±7.8 | 86.4±7.6 | 87.1±6.0 |
| **PE-SSFP** | PSNR | 55.1±3.9 | 61.4±6.1 | 59.9±5.3 | 58.3±3.7 |
| | SSIM | 83.8±10.0 | 86.2±8.8 | 86.7±8.2 | 89.0±6.0 |

Separate phantom images were simulated for varying $\alpha$, TR, $T_1/T_2$ parameters, and SNR values (for CSF). Each panel lists PSNR and SSIM measurements reported as mean±std across the varied parameter.

Supporting Table S5: Image Quality: Variations in Tissue and Sequence Parameters

| | | **N = 2** | **N = 4** | **N = 4** | **N = 6** |
|---|---|---|---|---|---|
| | | **R = 4** | **R = 6** | **R = 8** | **R = 8** |
| **ZF** | PSNR | 44.8±0.1 | 45.5±0.1 | 43.0±0.1 | 44.7±0.1 |
| | SSIM | 60.0±0.9 | 59.0±0.8 | 55.6±0.9 | 58.9±0.9 |
| **iCS** | PSNR | 54.1±0.4 | 53.5±0.4 | 50.0±0.3 | 49.4±0.3 |
| | SSIM | 96.4±0.1 | 91.8±0.3 | 88.4±0.3 | 88.4±0.4 |
| **ESPIRiT** | PSNR | 45.9±0.1 | 52.9±0.1 | 50.3±0.2 | 52.8±0.3 |
| | SSIM | 91.7±0.1 | 94.3±0.1 | 93.0±0.1 | 94.4±0.1 |
| **PE-SSFP** | PSNR | 56.4±0.3 | 69.1±0.3 | 61.4±0.3 | 63.4±0.3 |
| | SSIM | 97.0±0.1 | 97.6±0.0 | 96.6±0.0 | 97.5±0.0 |

Separate phantom images were simulated for varying undersampling factors (R) that are greater than the number of phase cycles (N). Each panel lists PSNR and SSIM measurements reported as mean±std across 10 cross sections.

Supporting Table S6: Image Quality: Acceleration Factor

## List of Supporting Figures

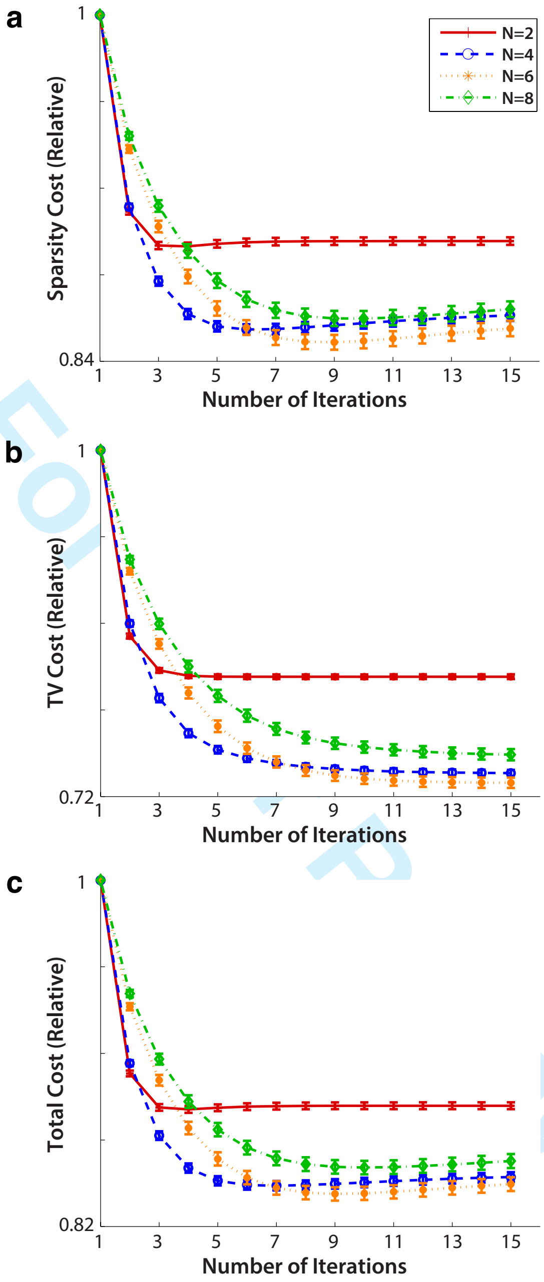

Supporting Figure S1: Undersampled acquisitions of the numerical brain phantom were reconstructed using PE-SSFP. The percentage difference between the reconstructed images in consecutive iterations fell to 0.001% within 15 iterations. The evolution of the PE-SSFP cost terms (calculated after the data-consistency projection) across these iterations are shown for N=2-8: **(a)** joint-sparsity cost, **(b)** TV cost, **(c)** combined cost in Eq. 6. The cost at each iteration is displayed as mean±std across 10 cross sections. The cost terms diminish smoothly across iterations.

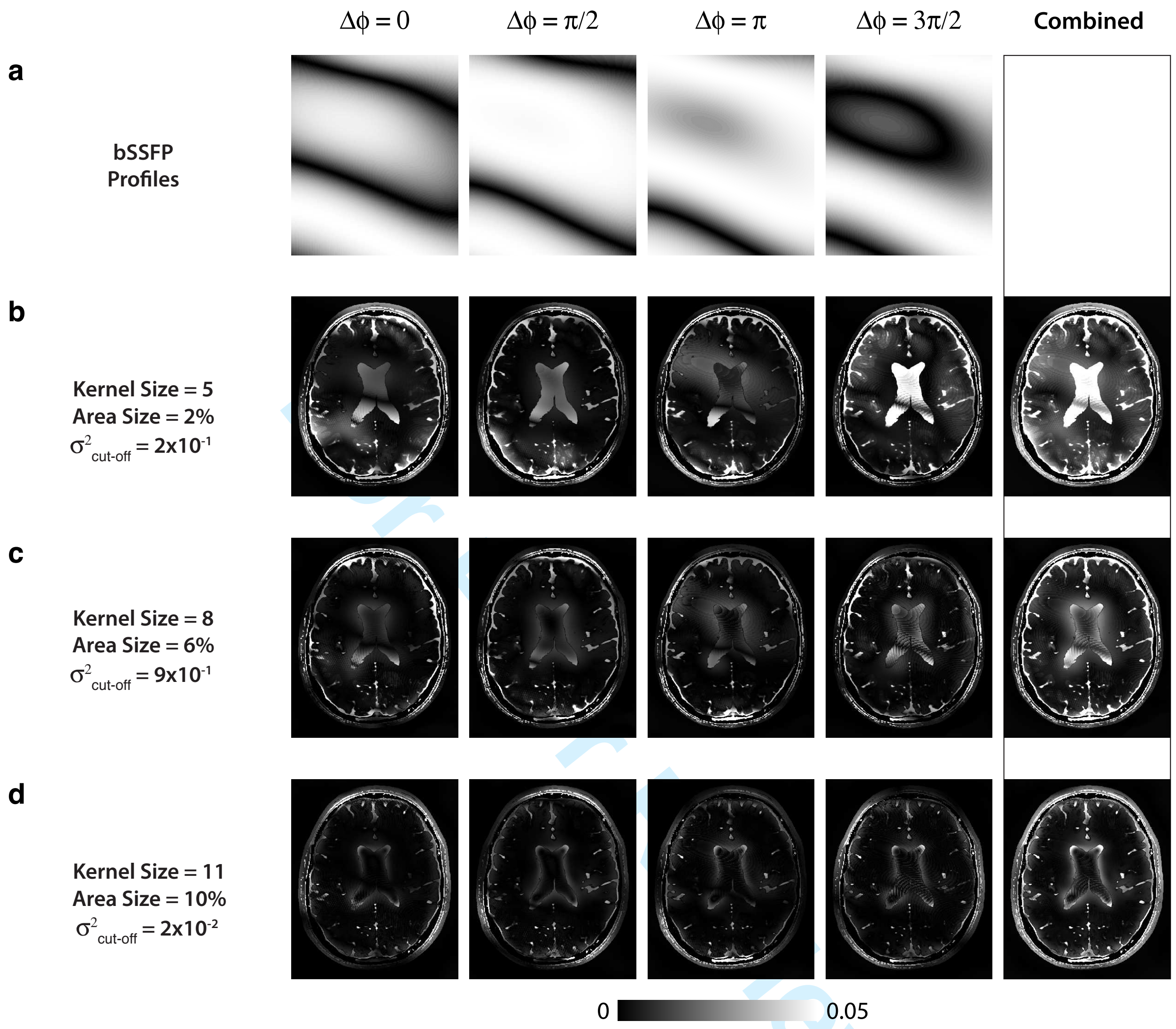

Supporting Figure S2: The auto-calibration approach was demonstrated by examining how well the acquired data can be represented via the bSSFP profiles estimated from calibration data. A separate error map was first calculated between the fully-sampled image at each phase cycle and its projection onto the subspace spanned by the bSSFP profiles. These individual error maps were then sum-of-squares combined across phase cycles. Representative maps are shown for N=4. **(a)** Actual bSSFP profiles for each phase-cycle. **(b-d)** Individual and combined error maps for varying calibration-kernel sizes ([5, 8, 11]), calibration-area sizes ([2%, 6%, 10%] of the maximum spatial frequency), and null-space cut-offs ($\sigma_{cutoff}$=2x10$^{-1}$, 9x10$^{-2}$, 2x10$^{-2}$). The relatively small calibration area/kernel size and high $\sigma_{cutoff}$ in **b** cause prominent low- and high-spatial-frequency errors, whereas the more optimal parameters in **d** (those used in PE-SSFP) significantly dampen the low-spatial-frequency errors. In all cases, relatively higher errors occur in the vicinity of banding artifacts in individual maps. Because banding artifacts for distinct phase-cycles are in non-overlapping locations, the combined maps show a rather uniform error distribution.

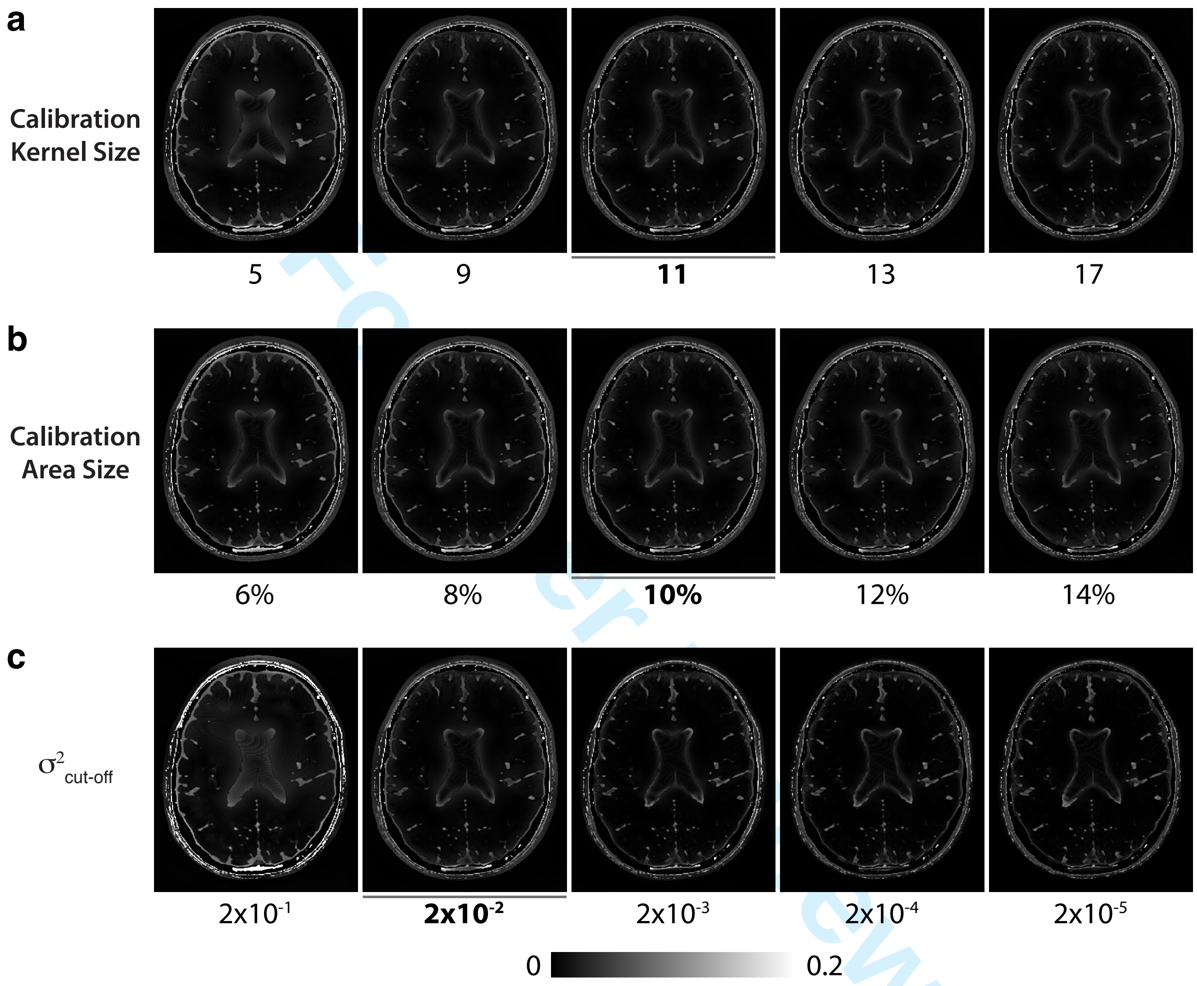

Supporting Figure S3: The success of the auto-calibration approach in estimating bSSFP profiles was analyzed for a broad range of calibration-kernel sizes, calibration-area sizes and null-space cut-offs. Representative error maps combined across phase-cycles are shown for N=8. **(a)** Error maps for different calibration-kernel sizes. **(b)** Error maps for different calibration-area sizes. **(c)** Error maps for different null-space cut-offs. PE-SSFP parameters are emphasized in bold font within each panel. The errors predominantly occur in regions of sharp signal transition near tissue boundaries.